ACS APPLIED NANO MATERIALS

www.acsanm.org Article

Zinc Oxide and Metal Halide Perovskite Nanostructures Having Tunable Morphologies Grown by Nanosecond Laser Ablation for Light-Emitting Devices

Nazrin Abdullayeva, Cigdem Tuc Altaf, Alihan Kumtepe, Nazmi Yilmaz, Ozlem Coskun, Mehmet Sankir,* Hamza Kurt, Cem Celebi, Alper Yanilmaz, and Nurdan Demirci Sankir*

Cite This: *ACS Appl. Nano Mater.* 2020, 3, 5881−5897 Read Online

ACCESS | Metrics & More | Article Recommendations | Supporting Information

ABSTRACT: This work reports a one-pot chemical bath deposition (CBD) method for the preparation of selectively grown, morphology-tunable zinc oxide (ZnO) nanostructures provided via straightforward nanosecond fiber laser ablation. Nanosecond fiber laser ablation is different from lithographic methods due to its simple, time saving, and efficient film scribing abilities. Here, multiple morphologies of the ZnO nanostructures on the same substrate have been grown via laser ablation of the ZnO seeding layer. Selective and controlled ablation of the titanium layer, ZnO growth inhibitor, resulted in systematic growth of nanorod arrays, while the application of extensive fluence energies resulted in the penetration of the laser beam until the glass substrate induced the nanoflake growth within the same CBD environment. The laser penetration depth has been numerically investigated via COMSOL Multiphysics heat module simulations, and the optical variations between two nanostructures (nanorod and nanoflake) have been examined via Lumerical FDTD. The simultaneous growth of two morphologies served as an efficient tool for the enhancement of photoluminescence intensities. It increased the average charge carrier lifetimes of the thin films from approximately 2.01 to 9.07 ns under the same excitation wavelengths. The amplification in PL performances has been accomplished via the capstone of all-inorganic halide perovskite (IHP) deposition that brought a successful conclusion to lifetime responses, which have been increased by 1.4-fold. The development of IHP sensitized nanoscaled multimorphological ZnO thin films can, therefore, be used as potential nanomaterials for light-emitting-device applications.

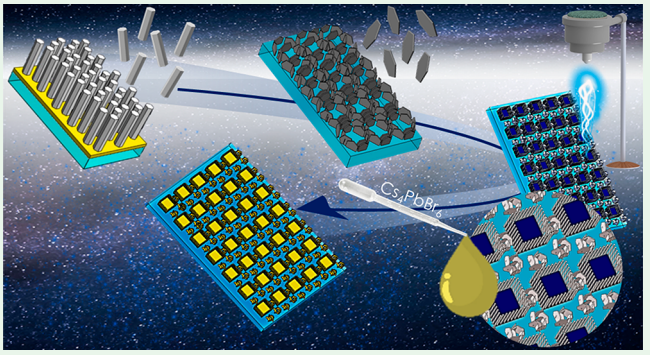

KEYWORDS: *ZnO photoluminescence, multimorphological ZnO, nanosecond fiber laser ablation, laser-assisted patterning, COMSOL heat distribution*

INTRODUCTION

The growth of ordered and arranged micro- and nanostructures on predetermined regions has demonstrated a significant enhancement in their material properties. To date, a large variety of patterning techniques have been reported in the literature among which template-based techniques, solvent assisted patterning, lithographic methods, such as e-beam, nanosphere, and nanoimprinting lithography, and atomic force microscopy nano machining are the most prominent ones.[1−4] Among the distinctive features of the patterned nanostructures, such as the generation of plasmonic colors, photonic band gaps, meta-surfaces, slow photons, the light manipulation ability is the one that has the most prominent impact on light associated applications.[5−10] Recent studies conducted in the field of photovoltaic, light-induced catalysis and optoelectronic devices have obtained fruitful outcomes in virtue of the patterning effect.[11−19] By establishing control over the shape, size, and distance between pattern features, the manipulation of photon behavior has been achieved. The research reported by Kang et al. has demonstrated improved field emission performance as a result of patterned zinc oxide (ZnO) growth via microcontact printing.[1] In another study, the photolithographic growth of nanocone structures has exhibited remarkable antireflective features.[20] Thus, due to the increasing interest in patterned micro/nanostructured arrays, the implementation of morphology-tunable ZnO has been pushed forward into this area as well.[21−23]

Received: April 18, 2020
Accepted: June 3, 2020
Published: June 3, 2020

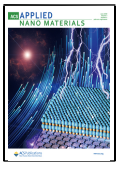

https://dx.doi.org/10.1021/acsanm.0c01034
ACS Appl. Nano Mater. 2020, 3, 5881−5897

As a successful representative of metal oxide semiconducting materials, ZnO has lately attracted lots of attention owing to its distinctive and characteristic features such as high surface-to-volume ratio, a large variety of 1D−3D micro/nanostructures, direct and tunable bandgap (3.37 eV), long-term stability, and eco-friendly nature. A vast diversity of ZnO application areas has been encountered heretofore of which photocatalytic/photoelectrochemical applications, piezoelectric devices, sensors, photodetectors, and LEDs are the most common ones.[24−30] Optical properties and luminescence abilities of ZnO have been intensely investigated via the inclusion of surface and bulk defects (doping) into material that resulted in the formation of midgap energy levels.[31−33] Moreover, the selected synthesis method and preferred crystal growth mechanism and orientation of ZnO have been proven to be highly effective on the defect density and, consequently, luminescence abilities. In one of the present studies, Yang et al. have investigated the differences in luminescence wavelengths of three differently synthesized ZnO nanoparticles and examined their effects on performances of organic photovoltaics.[34] The incorporation of different kinds of defects during distinct synthesis methods has been proposed as the main cause of luminescent color variation. Another study performed by Bora et al. analyzes the effect of annealing on hydrothermally grown ZnO nanorod (NR) arrays.[35] The study reveals a significant increase in the number of defect states up to 250 °C, while further heating resulted in defect passivation and a severe decrease in PL intensity.

By using a different approach to defect incorporation, Chanda et al. have analyzed the luminescence properties before and after cobalt doping.[36] All of the studies mentioned above have examined the PL properties of ZnO nanoparticles and continuous thin films. However, a limited amount of research has been reported on the distinguishable differences in the optoelectronic properties of selectively grown ZnO. For instance, Dai et al. have studied the changes in transmittance properties as a result of nanoimprint-lithography-based ZnO NR patterning.[37] Another study conducted by Hassanpour et al. investigated selective growth of NR via lithographic methods where a slight red shift has been observed as a result of patterning.[24]

Despite remarkable numbers of studies reported on the patterned growth of ZnO micro/nanoarrays in the literature, most of them are based on expensive and time-consuming lithographic methods. Although the resulting patterns are highly controlled and arranged, the reproducibility of these devices seems highly sumptuous. Therefore, novel, cost-effective, and time-saving patterning methods have been investigated lately.[22,38−41] One of the proposed methods by Murillo et al. focuses on the ZnO preference medium, where the nucleation and growth of the nanostructures take place on a certain seed layer comparatively faster than on the other thin-film layer.[40] The study reports that the growth of patterned ZnO nanosheet arrays on the growth promoter aluminum nitride (AlN) seed layer is 4 times faster than that on neighboring gold (Au) thin film. Although the given study has reported a highly successful selectivity, costly and time-consuming photolithography and lift-off techniques have been used to pattern AlN and Au films. Besides, optoelectronic properties of the resulting patterned thin films are remaining unclear and require further investigations.

Motivated by the ZnO growth medium preference, herein, we report a brand new, seed layer selective, multimorphological ZnO nanostructure formation technique through one-step hydrothermal growth. For the very first time in the literature, a nanosecond (NS) fiber laser has been applied on bilayer titanium/zinc oxide (Ti/ZnO) thin films for the selective ablation of the upper Ti layer at different fluence energies. The ZnO layer revealed as a result of controlled ablation is a promotive seed layer for fast and homogeneous NR growth, while the remaining Ti layer plays the role of ZnO growth inhibitor. Moreover, the delamination of thin film through the glass at higher ablation power throughput results in the growth of nanoflake (NF). Hence, a feasible ablation has been applied on the bilayer of Ti/ZnO coated substrates, where the growth of NF and NR structures has been concurrently maintained via one-step hydrothermal ZnO growth. The presence of multimorphologically grown ZnO in a selective manner on a single substrate has provided the composite photoluminescence (PL) peak formation.

Moreover, the combination of different luminescence wavelength regions provided by NR and NF structures is found as a suitable optical property for upcoming light-emitting, optoelectronic device cultivation studies. Additionally, mathematical modeling has been conducted to explain the rationale behind the laser ablation of ZnO/Ti thin films. More specifically, COMSOL Multiphysics Heat module simulations have been used to determine the effects of laser heating on the thin-film layers. Furthermore, Lumerical FDTD has been used to simulate the optical variations between NR and NF structures. Further enhancement in the light emission performance of the patterned ZnO thin films has been achieved via inorganic lead halide perovskite sensitization. Hence, the present study reports numerous novelties based on a smart and efficient way of maintaining patterned ZnO growth via NS laser ablation. Besides, easily patterned ZnO thin films embodying two different nanostructures have been decorated with a polycrystalline perovskite layer. For the very first time in the literature, their combined luminescence performances have been investigated. The notable increase in PL performances has turned the developed system into a strong potential candidate for future light-emitting device applications.

EXPERIMENTAL SECTION

Indium−tin−oxide (ITO) coated glass substrates have been purchased from Teknoma Technological Materials Industrial and Trading Inc. (Izmir, Turkey). Zinc oxide (ZnO, 99.99%) and titanium (Ti, 99.99%) sputtering targets have been procured from Plasmaterials, Inc. (California, USA). Zinc chloride ($ZnCl_2$) and hexamethylene tetraamine, $C_6H_{12}N_4$ (HMTA), purchased from Sigma-Aldrich (Schnelldorf, Germany) have been used as the zinc source and precursor, respectively. All chemicals have been used as received without further purification.

ITO coated glasses have been used as substrates for thin-film deposition. The principle was to create a double-layer thin film containing ZnO and Ti, consecutively, which provides different growth environments for CBD grown ZnO nanostructures. ZnO, playing the role of the seed layer (i.e., the growth promoter layer), has been deposited via RF magnetron sputtering (Vaksis Midas PVD-MT/2M2T, Ankara, Turkey) under an ultrahigh vacuum of 10^{-6} Torr in a chamber filled with 99.999% pure argon gas at 60 W for 6 min. The deposited ZnO films have been further annealed at 300 °C for 30 min under 13 sccm of N_2 gas flow. This step has proceeded with the sequential deposition of the Ti layer at 100 W for 16 min. ZnO nanostructure deposition has been performed in an aqueous solution of 0.03 M $ZnCl_2$ and 0.06 M HMTA at 80 °C for 3 h.

A ytterbium fiber laser with 1064 nm wavelength (FiberLAST, Ankara, Turkey) has been used for selective ablation. Detailed

https://dx.doi.org/10.1021/acsanm.0c01034
ACS Appl. Nano Mater. 2020, 3, 5881−5897

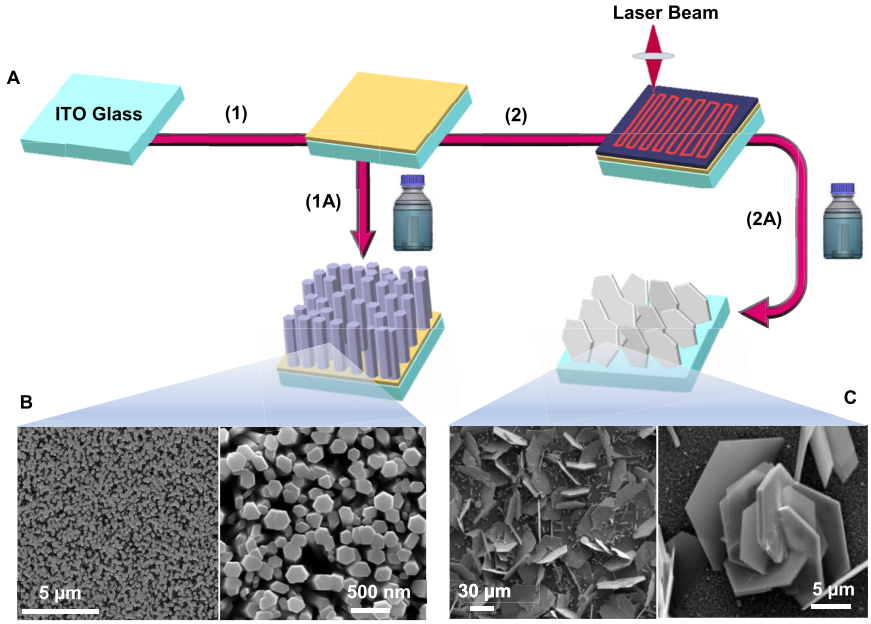

Figure 1. (A) Experimental process steps consecutively: (1) ZnO deposition via sputtering on ITO coated glass substrate followed by either (1A) CBD step for NR growth or (2) Ti deposition and laser hatching for (2A) NF growth via the same CBD solution. (B) Top view and magnified SEM images of NRs showing a homogeneous distribution of film throughout the substrate having a unidirectional orientation. (C) Top view and magnified SEM images of NFs showing a scattered distribution of film throughout the substrate having a dispersed orientation.

equations used in laser parameter calculations and basic device parameters (Table S1) are specified in the Supporting Information. Two fluence energy values have been selected for laser scribing which are (I) 28.43 J·cm^{-2} obtained under 25 W, 70 kHz, and 5500 mm·s^{-1} and (II) 3.72 J·cm^{-2} generated via 7 W, 150 kHz, and 4500 mm·s^{-1}. The initial ablation at high fluence energy has been applied in order to ablate the whole film from the surface, while the latter one represents more controlled scribing where the depth of the laser beam has been controlled up to the ZnO layer. SAM Light software has been used in order to sketch the ablation patterns for NS fiber laser scribing geometries.

$CsPbBr_3$ has been deposited on patterned thin films using the spin-coating technique. Briefly, a dimethylformamide (DMF) solution of 1.0 M $PbBr_2$ has been spin-coated onto the preheated, patterned thin films at 2000 rpm for 30 s, followed by drying at 80 °C for 1 h. Subsequently, a butanol solution of 0.07 M CsBr has been spin-coated on the $PbBr_2$ layer at 2000 rpm for 30 s and rinsed with isopropanol. Two different perovskite compositions have been obtained by varying the number of spin cycles of CsBr solution, where one cycle of CsBr spin-coating resulted in the formation of $CsPbBr_3$−Cs_4PbBr_6 composite crystals. In contrast, five cycles of CsBr deposition eventuated in pure Cs_4PbBr_6 crystals. Both films have been transformed into their final crystal form after being annealed at 280 °C for 10 min.

Morphological investigations have been carried out via scanning electron microscopy (QUANTA 400F Field Emission SEM). A Nikon Eclipse LV 150N optical microscope has been used to characterize the substrates after laser ablation steps and to maintain the control over the penetration depth of the laser beam. Crystalline structures have been thoroughly studied via X-ray diffraction and X-ray absorption fine structure spectroscopy (XAFS) analyses (SESAME (Synchrotron-light for Experimental Science and Applications in the Middle East), Allan, Jordan). Photoluminescence analysis has been conducted via a Horiba Jobin-Yvon Florog-550 photoluminescence (PL) system with a 325 nm line of a 50 mW He:Cd laser. Charge carrier lifetime measurements have been carried out via Edinburgh Instruments FLS1000 Spectrometer at KUYTAM (Koç University Surface Science and Technology Center, Istanbul, Turkey).

RESULTS AND DISCUSSION

The primary investigation has been commenced with the analysis of the resulting nanostructures grown in the same CBD solution containing $ZnCl_2$ and HMTA on two different substrates, which are ZnO seed layer deposited ITO glass and laser processed ITO/ZnO/Ti layer. ZnO and Ti thin films having thicknesses of 150 and 110 nm, respectively, have been deposited alternately via RF magnetron sputtering under an argon gas atmosphere at a high vacuum. The ZnO seed layer provides a favorable environment for easy and fast ZnO nanorod nucleation, while Ti plays the role of the ZnO nucleation retardant agent. Primarily, two control samples have been prepared to investigate the changes in the resulting nanostructures grown via CBD processes before and after laser ablation steps (Figure 1A). The given samples have been named as S1 for the pristine ZnO seed layer substrate and S2 for the laser processed substrate. More specifically, S1 had only a ZnO seeding layer deposited on ITO coated glass. On the contrary, S2 consisting of seriatim ITO/ZnO/Ti layers has been fully scribed under the applied fluence energy of 28.4 J·cm^{-2} (25 W and 70 kHz), which is the maximum energy provided by our laser system. The calculations for the fluence energy and applied laser parameters have been given in the Supporting Information (eqs S1 and S2). SEM images given in Figure 1B show the formation of the hexagonal NR arrays grown on the pristine ZnO seeding layer (S1). As can be seen from the given SEM image, the distribution of rods throughout the substrate is highly dense, with an average diameter of approximately 350 nm. On the other side, Ti coating and laser scribing of the surface provided the formation of 2D-hexagonal ZnO NF (Figure 1C). Besides, the obtained film formation throughout the substrate is not as dense as in the preceding sample, as the orientation of individual NFs is not homogeneous. It can be observed from the provided SEM outcomes that certain regions of the film appear to be quite bold.

https://dx.doi.org/10.1021/acsanm.0c01034
ACS Appl. Nano Mater. 2020, 3, 5881−5897

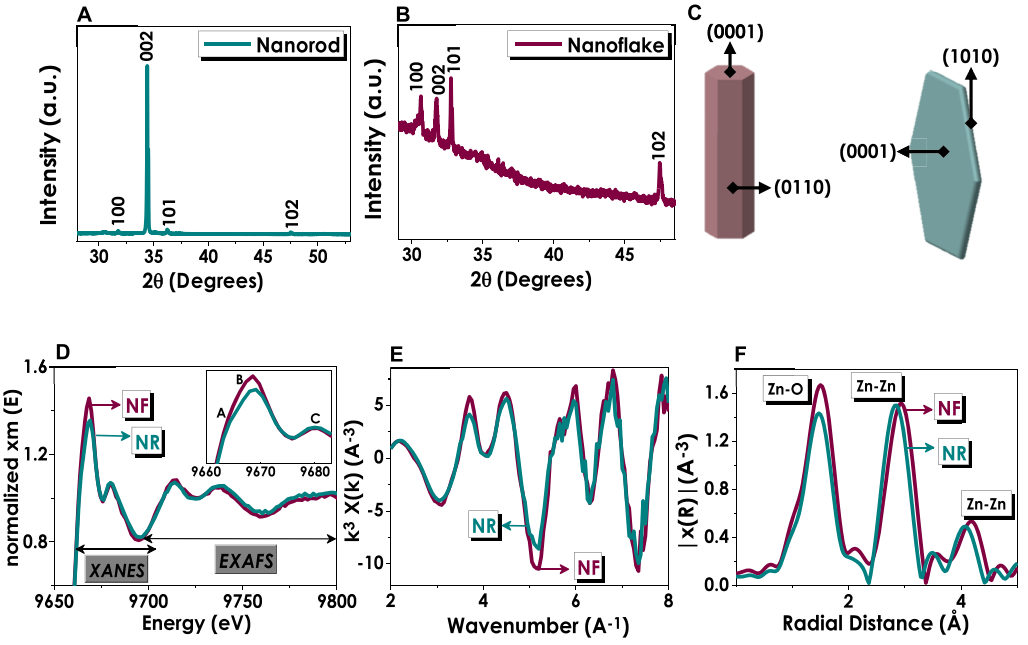

Figure 2. XRD spectra of wurtzite (A) ZnO NR with a strong [002] diffraction peak denoting the *c*-axis orientation and (B) ZnO NF with a hump at smaller diffraction angles appearing due to bare soda-lime glass substrate. (C) Schematic representation of rod and hexagonal flake structures and their facets. (D) XAFS, (E) XANES, and (F) EXAFS spectra obtained from NR and NF samples for detailed investigation of crystalline material properties.

In contrast, other regions contain agglomerated flakes revealing distinct formations as in the magnified image. EDAX results obtained from both NR and NF structures have been additionally specified in Figure S1 as interpretive data showing the characteristic differences in Zn:O ratios between two nanostructures. More specifically, the NR had Zn rich character, while the NF had O rich character.

Further characterizations of the NR and NF structures have been performed via X-ray diffraction (XRD) and absorption analyses. XRD patterns of the resulting nanostructures are given in Figure 2A and B. As evidenced by SEM images, a significant difference can be observed between the homogeneities and continuities of NR and NF thin films, where NR film formation appears to be much denser and uniform throughout the substrate. In comparison, NF formations generate a more dispersed and non-homogeneous film structure. XRD analysis of both thin films proves the presence of hexagonal wurtzite ZnO structure due to its characteristic diffraction peaks at [100], [002], and [101] crystallographic planes.[42] NR film formation has revealed its most substantial diffraction peak at the [002] plane approving the thin film's one-directional (*c*-axis) growth preference. In comparison, XRD patterns obtained from NF films confirm the less dense thin-film formation due to significantly smaller diffraction peaks at low angles, which corresponds to the amorphous nature of soda-lime glass substrate and comparatively lower wurtzite hexagonal ZnO peak intensities.[43]

Further investigations of the crystalline properties and electronic structure of ZnO thin films have been conducted via X-ray absorption fine structure spectroscopy (XAFS). The given analyses serve for two types of detailed material property investigations: (I) X-ray absorption near edge structure (XANES) provides information about the chemical environment (magnetic and charge states, chemical bonding, etc.) of elements, and (II), extended-XAFS (EXAFS) focuses more on a local arrangement of atoms providing quantitative information such as coordination number and bond lengths.[44]

XANES spectra obtained from NR and NF are illustrated in Figure 2D with a corresponding inset focusing on the 9660−9680 eV range. The given inset figure specifies a slightly noticeable shoulder and three main peaks, labeled as A (9664 eV), B (9669 eV), and C (9680 eV), respectively, which can be attributed to the excitation of Zn core electrons from 1s to the unoccupied 4p states.[45,46] Comparing the XANES spectra for two nanostructures individually, a distinguishable difference can be observed at the maximum intensities of electric field vector **E** of X-rays, where NF generates higher absorption compared to that of NR. Additionally, a tiny shift in the eV values of peak B can be attributed to differences in the local band structure of NRs absorbing X-rays with their (0001) facets having an average diameter of 350 nm. In comparison, NFs having a random structural orientation reveal both (0001) and (1010) planes with micron-sized features and therefore contribute to stronger absorption (Figure 2C). Figure 2E represents the k^3- weighted $\chi(k)$ EXAFS results obtained as a result of atomic background extraction from XAFS spectra via computer-aided ARTEMIS and ATHENA software for the detailed investigation of the local atomic structures. To quantitatively examine and compare the structural differences between ZnO NR and NF structures at Zn K-edges, the obtained EXAFS data has been Fourier transformed, as given in Figure 2F.

The overall data is in good agreement with previously reported wurtzite ZnO spectra, where the primary peak at around 1.5 Å is generated as a result of the contribution of the four closest oxygen atoms (first coordination shell) surrounding the absorbing Zn atom.[46−48] The second strong peak at approximately 2.9 Å originates as a result of outer coordination shells formed in between 12 neighboring Zn atoms. Performing the individual comparison between two nanostructures, the

https://dx.doi.org/10.1021/acsanm.0c01034
ACS Appl. Nano Mater. 2020, 3, 5881−5897

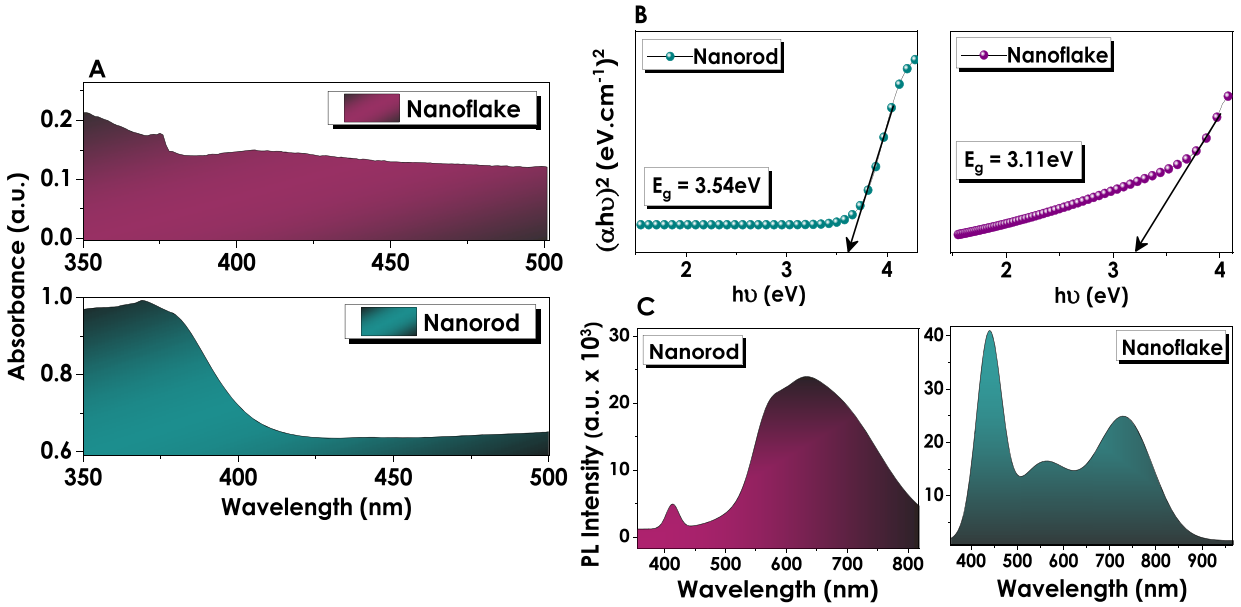

Figure 3. (A) UV−vis spectra of NF and NR samples showing a comparably stronger absorptivity performance in NRs than NFs throughout the analyzed spectrum. (B) Tauc plots for band gap evaluations calculated from transmittance data. (C) Photoluminescence spectra of samples with two completely different luminescent behaviors generated due to the varying defect densities.

first peak representing the Zn−O bond length appears at 1.47 and 1.50 Å for NR and NF, respectively. In addition to the significant shift in the radial distance of Zn−O bonding, there is also a noticeable enhancement in the intensity of the reflecting wave from NF. A much more distinguishable shift can be observed for Zn−Zn bond lengths for two different nanostructures, where the measured lengths for NRs are 0.1 Å shorter than those of NFs. It is indeed the shift in the outer coordination shells that informs us more about the strain changes in the ZnO epilayer and therefore provides more knowledge based on the nanostructure variations. In other words, the slight shifts observed for Zn−Zn bond lengths of NR and NF structures approve the effect of changing morphology on local structural and electronic arrangements.

The optical characterizations of NR samples have been done via UV−vis analysis, and the obtained absorbance data is given in Figure 3A. The dense NR film structure contributed to intense absorption behavior, while non-homogeneous NF film formation resulted in a scanty optical performance. Besides, NR films designate a strong absorptivity in the UV region with a severe decrease at wavelengths >400 nm. Optical characterization data has also been used for the evaluation of bandgap (E_g) values through the Tauc plots given in Figure 3B by intersecting the linear region of the plots on the *x*-axis. The given plots have been evaluated by using transmittance data and thin-film thicknesses, both specified in Figure S2. It has been calculated that the bandgap of the NF, 3.11 eV, was smaller than that of NR samples, 3.54 eV.

Photoluminescence (PL) of NR and NF structures possesses individual significances due to the completely different luminescence behaviors of the thin films (Figure 3C). The excitation has been conducted via a 325 nm (3.81 eV) He:Cd laser source that possessed sufficient energy for the electrons of both ZnO nanostructures to be excited from the valence to the conduction band. It is also noteworthy to say that, under the mentioned laser excitation, NF and NR films have produced a bluish and yellowish luminescence, respectively, as can be seen in Figure S3. The PL spectra obtained from pristine NR thin films exhibit two emission peaks located at 410 and 630 nm wavelengths, respectively. The primary peak corresponds to the near-band-edge emission (NBE) generated as a result of the radiative recombination of excitons.[49] The reason for the NBE peak appearing at wavelengths >400 nm can be attributed to the wide bandgap of synthesized ZnO NRs (Figure 3B). Moreover, it has been previously reported that the dimensions of NRs show a remarkable effect on their NBE peak positions having a blue shift at decreasing diameters and a red shift at increasing diameters.[50] The second peak appearing in a broad visible wavelength range reaches its maximum emission at 630 nm and contains a slight shoulder at approximately 580 nm. The visible emission range is being attributed to as the region of emission caused by defects (i.e., defect-based emissions, DBE) present in the ZnO crystal structure.[33,51,52]

The comparably low intensity of the NBE concerning DBE can be attributed to nanoscale dimensions (∼350 nm) of NR samples resulting in an increased number of scatterings on the surface. PL spectra of NF samples, per contra, have three different PL emission peaks of approximate intensities comprising almost the whole visible region. Compared to NR, PL intensities of NF appear to be much higher, signifying a different defect mechanism within the structure, which requires a more detailed investigation. The appearance of the NBE peak at ∼430 nm, which is slightly red-shifted compared to other NBEs reported in the literature, can be attributed to a smaller bandgap of NF structures.[53] Additionally, the variation in the concentration of native defects can also be responsible for the shift in the NBE peak of ZnO NF. Several studies reported on defect contents in ZnO have indicated that the number of defects on the surface is higher than those existing within the bulk volume.[54,55] Hence, it can be concluded that the varying surface-to-volume ratio of each nanostructure has a certain effect on its surface defect density.

Therefore, a more specific inspection of PL emissions has been conducted through the deconvolution of the obtained spectra. The PL responses of both nanostructures have been fitted into three corresponding Gaussian peaks named as O1,

https://dx.doi.org/10.1021/acsanm.0c01034
ACS Appl. Nano Mater. 2020, 3, 5881−5897

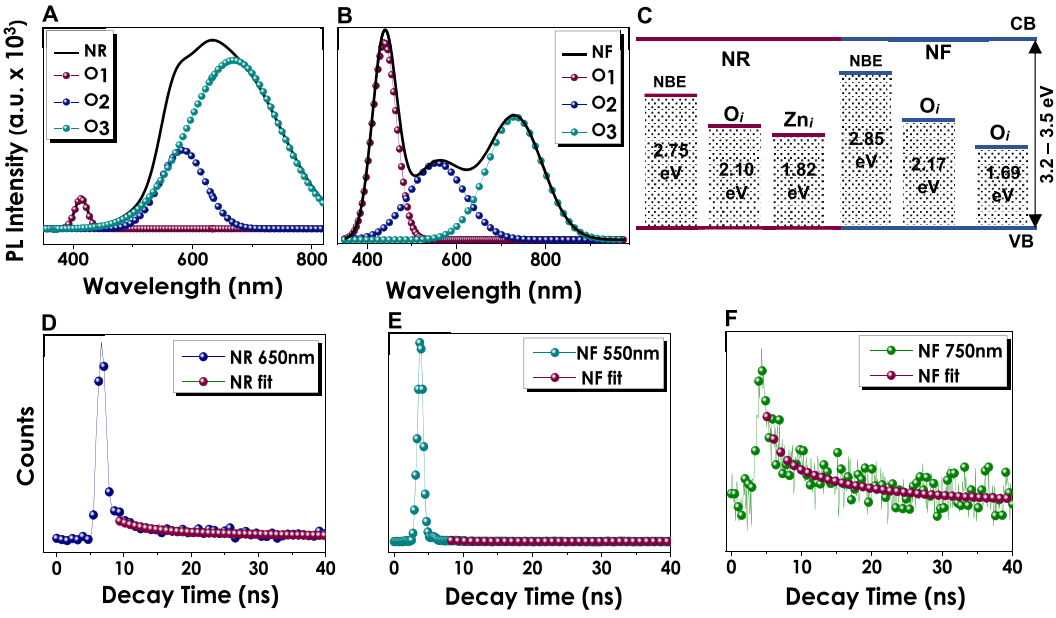

Figure 4. PL deconvolutions of (A) ZnO NR and (B) ZnO NF samples into three Gaussian peaks each corresponding to a certain defect parameter specified in (C) the scheme. TrPL spectra of (D) NR collected at 650 nm corresponding to the defect generated emission wavelength of sample and of (E, F) NF obtained at two strong defect-based emissions.

O2, and O3, respectively (Figure 4A and B). Analyzing the Gaussian fits, it can be concluded that O1 peaks in both NR and NF structures appear in the NBE region that is a type of non-defect-related emission. However, O2 and O3 peaks are all individual representatives of defect associated emissions in ZnO nanostructures residing within the visible and NIR regions. The Gaussian bands deconvoluted from PL spectra of NR samples reveal O2 and O3 peaks at 580 and 660 nm, respectively, representing the orange and red emissive nature.[56] Taking a closer look at the DBE wavelengths, it can be specified that the shoulder appearing at 580 nm corresponds to the orange emission region and has been reported to signify the radiative recombination between the electrons and holes that are trapped in the oxygen interstitials.[57]

According to a previous study conducted by Gheisi et al., it has been suggested that the oxygen atoms being absorbed on the ZnO surface induce band bending and push the photogenerated holes toward the surface.[58] By this mechanism, the holes are being trapped on the surface via Oi and contribute to a surface-based emission. The emission peak at 630 nm, on the other hand, is located in the red region of defect-based emissions and has been reported to stand for zinc interstitials (Zni) that originate from lattice disorders along the *c*-axis of NRs. However, in order to approve our remarks, the XPS spectra of NRs have also been investigated (Figure S4). The obtained O 1s peak has been deconvoluted into three fitting Gaussian peaks residing at low, medium, and high binding energy levels, respectively.[59] The oxygen in the Zn−O lattice (O1), oxygen vacant regions (O2), and chemisorbed oxygen (O3) resulted in these peaks.[42] The O3 peak residing at high binding energies is representing oxygen interstitials that are formed as a result of oxygen chemisorption on the ZnO surface. The intensity of the O3 peak is significantly lower compared to the one representing oxygen vacancies within the structure.

However, the O 1s spectrum can only classify the types of oxygen-related defects. Still, it cannot distinguish zinc interstitials from oxygen vacancies.[60] Therefore, in order to prove that the second PL emission in the red region is Zni related, the XPS spectrum for Zn 2p has also been analyzed. As a primary step, the binding energy difference between two components of Zn 2p has been evaluated as 23.1 eV, which is in good agreement with previously reported energy separation values.[61] Further, each peak has been deconvoluted into three fitting Gaussian peaks with corresponding binding energies given in Figure S4B. Both Gaussian peaks of Zn $2p_{3/2}$ and Zn $2p_{1/2}$ residing at lower energy levels signify metallic Zn present within the nanostructure. The energy difference between middle peaks corresponding to 23.2 eV affirms that the corresponding peaks stand for lattice Zn due to the favorable value of the spin−orbit splitting of divalent Zn atoms. Analyzing the final peaks located at higher energy levels, attention needs to be paid to the binding energy values that are going to have a determinant character for the validation of the presence of Zni.

According to the literature review, the energy values of our samples (1023.5 and 1046 eV) obtained from Gaussian deconvolution of Zn 2p are considerably high. This denominates that Zn atoms are at the interstitial position being surrounded by more than one oxygen.[61] Thus, the obtained XPS results are in accordance with the remarks made on types of defects of ZnO NRs. Moreover, the EDAX data obtained from NRs (Figure S1) shows the dominance of Zn over O atoms in atomic weight percentage. These results appear to be in good agreement with the deconvoluted Gaussian peak ratios obtained from NRs, showing the superior intensity of Zni over Oi representing peaks.

The deconvolution spectra of NFs show Gaussian peaks with similar intensities. The stronger emission of the NBE peak in the UV region can be attributed to a larger surface area of NFs.[54] The primary deconvoluted peak appears at 570 nm, which is located within the yellow emission range that represents Oi in the structure. The contradictive part of the given NF PL spectra lies in the second deconvolution obtained at 730 nm. This emission is within the near-infrared (NIR) range, which has been studied by various research groups, but

https://dx.doi.org/10.1021/acsanm.0c01034
ACS Appl. Nano Mater. 2020, 3, 5881−5897

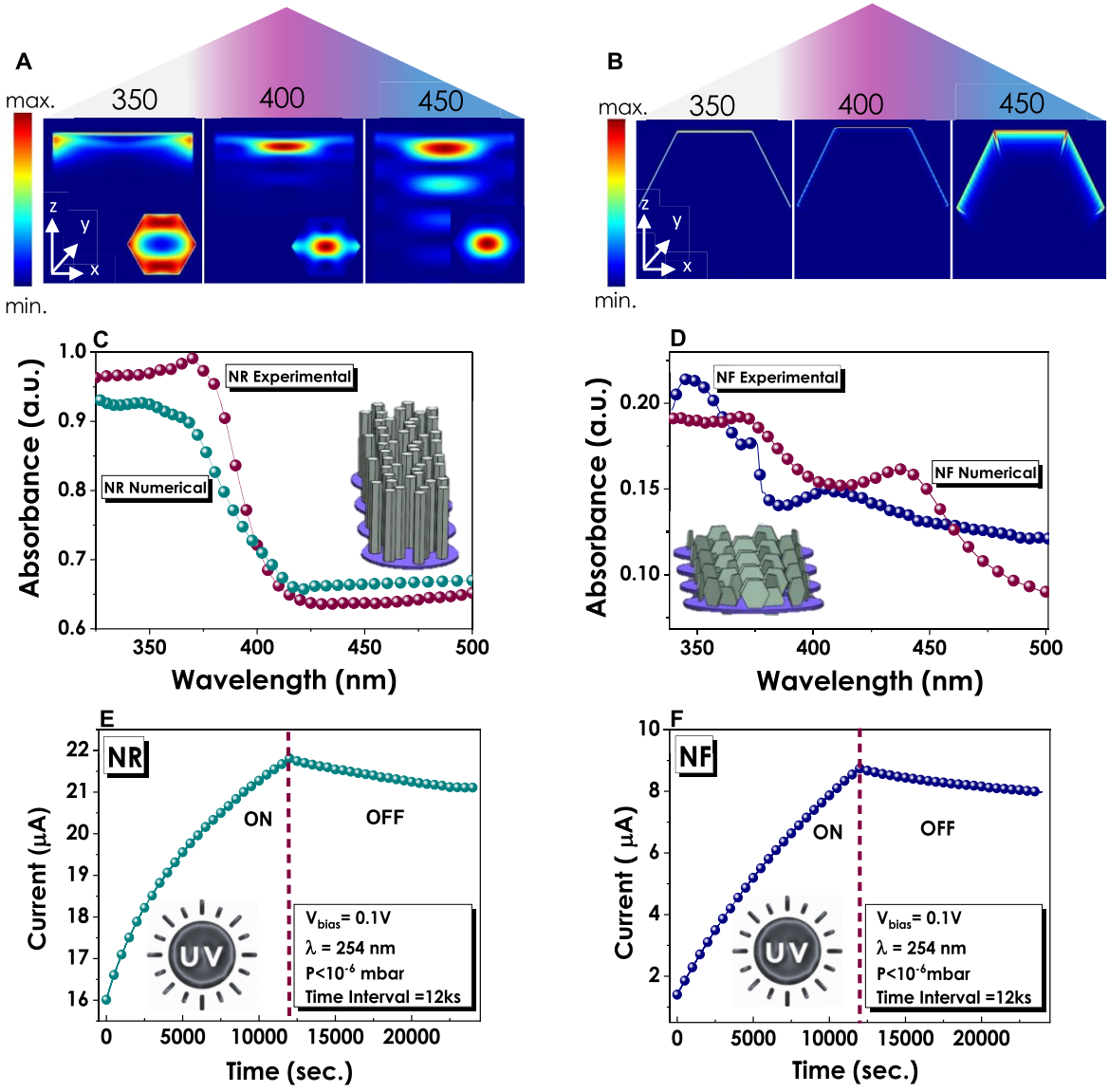

Figure 5. FDTD simulations of absorption behavior of (A) ZnO NR with cross and top view images and of (B) ZnO NF showing a reasonable absorbance within their bandgap values. Individual comparison of numerical absorbance data obtained from simulation with experimental results for (C) NR and (D) NF. TPS plots obtained under UV illumination in an ultrahigh vacuum followed by a gradual decrease under light obscureness measuring the light responsivity of (E) ZnO NRs and (F) NFs.

the eventual cause of luminescence has not been precisely detected. The closest approach has been proposed by Wang et al., where the formation of NIR emission has been correlated with the presence of Oi states.[62] It has been reported that NIR emission is originated from the radiative recombination of electrons trapped in shallow levels with deeply trapped holes at oxygen interstitials.

Time-resolved photoluminescence (TrPL) has been conducted to investigate the charge extraction and coupling mechanisms of NR and NF structures and to correlate them with the defect contents. Figure 4D–F shows the TrPL spectra and their corresponding fits obtained at 344 nm picosecond laser excitation for NR and NF, respectively. The obtained fits disclose two lifetime components (τ_1 and τ_2) for NR, proving the double-exponential decay behavior. Analyzing the individual TrPL for NRs collected at 650 nm DBE wavelength, the initial PL rise has an instant response within 5 ns, reaching its maximum luminescence value at 6.48 ns. The decay of the corresponding nanostructures is fitted into two components of 4.52 and 53.33 ns duration. Given lifetime values represent a significantly fast primary decay followed by a slow decay showing a lingering charge recombination period. Considering the deconvoluted PL spectra of NRs, a correlation can be constituted between decay periods and defect states (Oi and Zni). Han et al. have previously reported that the fast recombination of minority charge carriers is mostly related to localized excitons generating the NBE peak.[63]

However, the slow recombination component can be attributed to deep level electrons that are formed via Zn and O interstitials. TrPL analyses for NFs have been collected at 550 and 750 nm values, which correspond to the two primary defect-based emissions obtained via PL analyses. The maximum photoluminescence intensity has been reached within ~3.8 ns for both emission wavelengths, showing a significantly faster reaction to the excitation laser source. However, an individual comparison between two wavelengths

https://dx.doi.org/10.1021/acsanm.0c01034
ACS Appl. Nano Mater. 2020, 3, 5881−5897

shows more rapid recombination of charge carriers collected at 550 nm in contrast to 750 nm, which possesses double-exponential decay. It has been previously discussed that the emission in the yellow region is originated due to the Oi.

In contrast, NIR emission is caused by radiative recombination taking place between shallow electrons and holes generated by Oi. Therefore, the fact that the monoexponential decay of NF at 550 nm and the primary decay component at 750 nm have approximately similar recombination lifetimes may refer to the recombination of electrons with midgap energy levels generated as a result of Oi. On the other hand, the slower recombination parameter at 750 nm might be caused by the indirect recombination of shallow electrons with deep holes formed due to the presence of Oi as mentioned above. The evaluated decay periods for NR and NF collected at predetermined wavelength values according to the PL emission spectrum have been specified in Table S2.

Finite-difference time-domain (FDTD) simulation has been conducted as an additional computer-aided characterization method, via Lumerical FDTD software, to investigate the absorption mechanism of ZnO NR and NF samples. The purpose was to establish and simulate the absorption behavior of highly continuous NR and less dense NF films and to correlate them with the obtained experimental results. The refractive index used during the absorbance simulations of ZnO nanostructures has been extracted from a previously conducted study.[64] The average length of 2.4 μm and the average radii of 175 nm have been set as structural parameters for NR design during the simulation. On the other hand, 240 nm average thickness, length varying within the 6−12 μm range, and an average 14.2 μm length of the long diagonal have been specified as necessary dimensional parameters for the simulation of NF absorption behavior (Figure S5A). As can be seen from the previously given SEM images (Figure 1), the orientation of NFs throughout the substrate is not homogeneous. Therefore, during the simulation, the angle between flake and surface has been varied in the z-axis within the 45 to −45° range.

It is also important to note that, during the simulation of the absorption behavior of NRs, the corresponding thicknesses of ITO/ZnO coated glass substrate have been specified as 100 and 150 nm, respectively. However, NFs are grown on a laser-ablated glass substrate, so there is no ITO/ZnO remaining beneath. Therefore, during the absorption simulation of NFs, the substrate has been selected as pure soda-lime glass. Analyzing the obtained results under three different wavelength values (350, 400, and 450 nm) given in Figure 5A and B, it can be interpreted that the light striking in the UV region does not propagate too much into the structure and is mainly absorbed in the upper layer of both rod and flakes. Both absorption maps represent the light penetration profile in the c-axis, while additional inset figures given for NRs show the absorption behavior at (0001) facets, as well. The increasing wavelength, consequently decreasing energy, results in a deeper propagation of light into the material. Although for NRs the penetrating light inside a single rod is much more distinguishable at 400 nm than at 350 nm, the difference is not so obvious for NFs.

It can be even suggested that, for NFs, the absorption at the surface has remained almost invariable at both 400 and 350 nm wavelengths. These results are found to be in good agreement with E_g values evaluated from Tauc plots (Figure 2) that show a better absorption behavior of both NR and NFs at their band gaps of 3.54 eV (350 nm) and 3.11 eV (399 nm), respectively. Interpreting the absorption maps obtained at 450 nm (2.75 eV), it can be concluded that the applied light is out of the absorbable wavelength range and therefore moves deeper into the material without being absorbed. Figure 5C and D represents the quantitative equivalents of the reported absorption maps showing a strong absorption performance at the UV region with a gradual decrease >400 nm. It is also essential to point out the consistency existing between experimental and theoretical absorbance values, proving the proximity of the simulation environment to the actual conditions. In addition to the performed numerical analyses, the effect of NFs' varying size on the eventual absorption behavior of thin film has been investigated.

This step has been conducted in order to detect the NF dimensions, which better approach the experimental absorbance values. The long diagonal (d) of NFs has been selected as the determinant size parameter. The length of d has been altered for the examination of changes in the absorptivity of the thin film. The given parameter has been varied between 12 and 16 μm, and the resulting absorbance spectra have been specified in Figure S5B. It can be seen that the absorptivity of NFs significantly increases throughout the analyzed wavelength region. Despite the scanty distribution of ZnO NFs, the enlarged dimensions of individual flakes increase the probability of light incidence directly onto the material and therefore have a stronger contribution to their light capturing ability. However, comparing all of the UV−vis performances of NFs simulated at different dimensions with the performance of the actual thin film, it can be concluded that diagonal lengths of 12 and 13 μm are too small, thus generating a lower absorptivity. On the other hand, 16 μm turns out to exceed the actual NF dimension, resulting in higher performances. Therefore, it can be concluded that, at d = 14−15 μm, the closest approach to the actual NF absorption performance has been attained.

Transient photocurrent spectroscopy (TPS) has been conducted to examine the photoresponsive characteristics of ZnO thin films under high vacuum conditions at 254 nm UV light. In order to remove atmospheric adsorbates, samples have been illuminated under the same light source for 2 h at $P \sim 10^{-6}$ mbar vacuum before the measurements. Özdoğan et al. have previously reported that the presence of both physisorbed and chemisorbed molecules on the surface has a significant impact on the resulting time-dependent photocurrent measurements.[65] Therefore, it has been concluded that the presence of an ultrahigh vacuum is not enough for the removal of adsorbates, and only under the effect of a severe energy source, such as UV light, a factual TPS response can be attained. During the analysis, the UV light has been kept "ON" for 12 ks and further switched "OFF" for 12 more ks in order to observe the relaxation process. As can be seen from Figure 5E and F, due to the generation of electron−hole pairs, NRs have primarily shown a severe current increase under the applied UV light, followed by a comparably slower advancement of current due to the desorption of adsorbed molecules from the surface.

A slow decay trend has been observed during the 12 ks period for both nanostructures under the UV "OFF" condition. When the UV light is turned off, the adsorbates, such as O_2 and H_2O with lower partial pressure in the middle of a 10^{-6} mbar vacuum range, tend to stick back onto the surface of ZnO nanostructures and, hence, give rise to a slight decay in the

https://dx.doi.org/10.1021/acsanm.0c01034
ACS Appl. Nano Mater. 2020, 3, 5881−5897

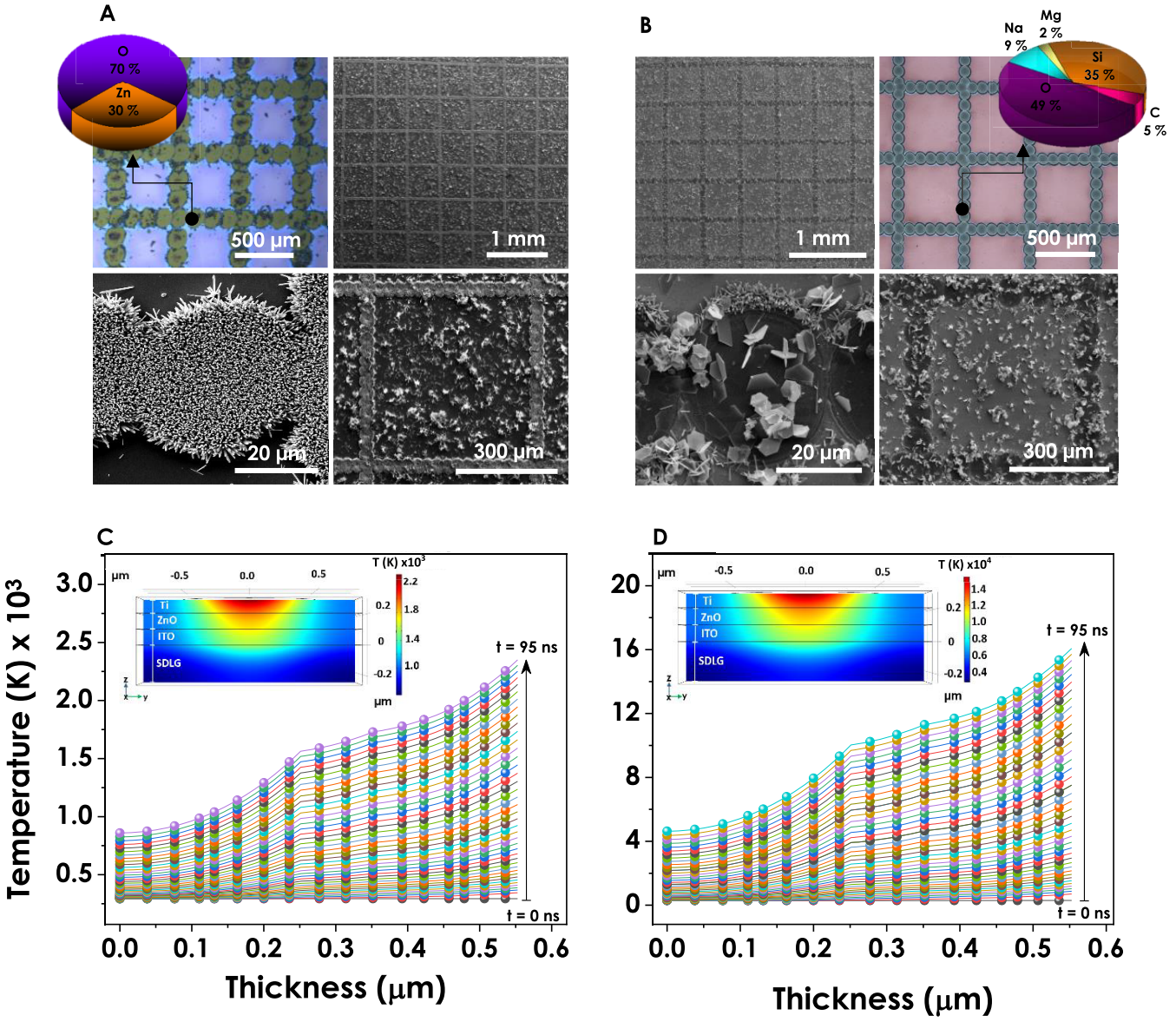

Figure 6. Investigation of NS laser scribed Ti/ZnO/ITO samples in a grid-like patterned manner via OM, SEM images and Comsol Multiphysics simulation—heat transfer module. (A and B) OM images obtained from 3.7 and 28.4 J·cm^{-2} fluence energy ablated, laser patterned bare samples with their corresponding SEM images at various magnifications showing (A) pristine ZnO NR growth under low fluence energy application due to controlled ablation of the upper Ti layer and (B) NR−NF combined multimorphological nanostructure growth obtained under high fluence energy application. (C and D) Computational simulation plots of temperature distribution throughout the film thickness with respect to time under (C) 3.7 J·cm^{-2} and (D) 28.4 J·cm^{-2} fluence energy.

measured current by capturing a portion of photogenerated electrons. It was found that, even after a period of 12 ks, the current of the sample could not reach its initial value measured before the UV light illumination. Comparing the TPS responses of NRs and NFs individually, a distinguishable difference in the amount of generated current (∼12 μA) under UV light can be observed. The reason behind this difference can be correlated with the light-exposed surface area of the samples.

Homogeneously oriented NRs effectively capture light-generating higher current density rather than randomly dispersed NF films. Besides, focusing on the individual differences between the illuminated and dark current responses of NRs and NFs, a stronger photoresponsivity has been detected for NF structures. One of the studies conducted by Sarkar et al. investigated the changes in TPS responses of ZnO NRs with the increasing rod diameter.[66] It has been observed that thinner rods, having a higher surface-to-volume ratio, result in better photoresponsivity bringing about faster responses to illuminations. When the diameter of rods increases from 25−50 to 150 nm, the photocurrent gain dramatically drops. This drop has been attributed to the densely packed structure of nanorods that inhibits the photogenerated current relaxation.

In our study, the average diameter of nanorods has been measured as ∼350 nm, thus resulting in a dense thin-film formation that cuts down photoresponsivity. In contrast, NF films are less densely packed, and therefore, the photocurrent relaxation takes place much faster. However, the disordered and dispersed film homogeneity limits the light absorption capacity. Resistance measurements have been conducted for both samples under "ambient air-in dark conditions" (C1) and

https://dx.doi.org/10.1021/acsanm.0c01034
ACS Appl. Nano Mater. 2020, 3, 5881−5897

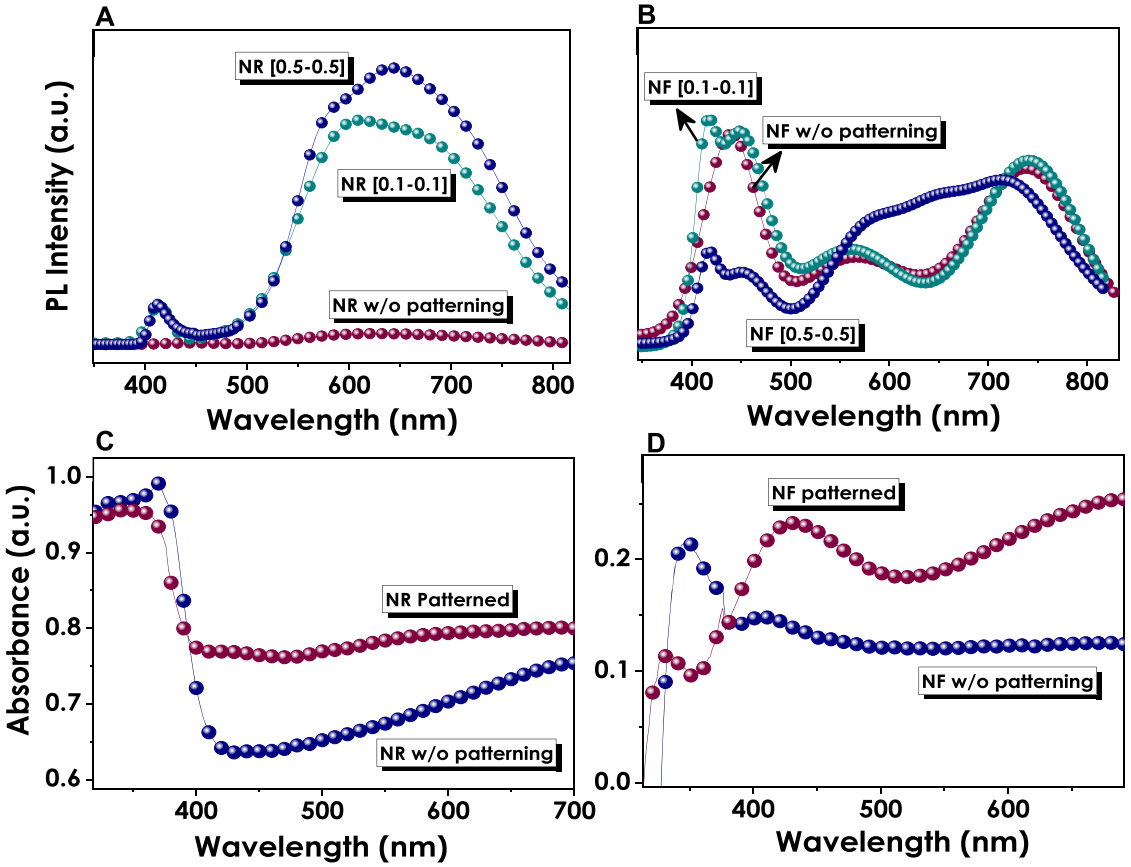

Figure 7. (A) PL spectra of pristine, 0.1 × 0.1 cm^2, and 0.5 × 0.5 cm^2 patterned NR samples showing a severe increase in intensities as a result of selective growth. (B) PL spectra of pristine, 0.1 × 0.1 cm^2, and 0.5 × 0.5 cm^2 patterned NF samples exhibiting a variation in PL behavior as a result of simultaneous NF/NR growth. UV−vis responses obtained from (C) NRs and (D) NFs prior to and after patterning.

"in vacuum-under illumination conditions" (C2), and obtained data has been specified in Figure S6. The distinguishable variation between C1 and C2 has been observed for both samples, mainly caused by the presence of UV light possessing necessary energy for the current generation. Individual comparison between C1 and C2 parameters for NRs shows a slight decrease in resistance as a result of UV illumination, which can also be explained by poor light responsivity but good conductivity of the samples. NF samples, on the other hand, show a remarkable change after light exposure, which agrees with their previously given light responsivities (Figure 5F). The resistance of NF, which is extremely high (MΩ) at C1, decreases by 10^3 orders of magnitude under C2 conditions. The reason behind these sharp responses toward illumination can be correlated with the light-exposed surface-to-volume ratio of the samples.

Following the detailed material characterizations of pristine NR and NF films, our study has evolved to a brand-new phase where the selective growth of either one or both structures has been maintained via nanosecond fiber laser ablation. ITO/ZnO/Ti deposited glass substrates have been subjected to two different laser beam energies. The fluence energy of the applied laser beam is calculated by the ratio of pulse energy divided by the area of the spot size. Equations that are used for energy calculations are specified in the Supporting Information in detail. Power, frequency, and scan rate are variables used in these equations. In our study, the selection criteria for the applied fluence energy are based on either selectively etching the upper Ti layer (~120 nm) without damaging ITO/ZnO beneath or completely ablating the whole film until the glass. Figure 6A gives the optical microscope (OM) images of the laser ablation process conducted under 7 W, 4500 mm·s^{-1}, and 150 kHz applied system parameters (3.7 J·cm^{-2}) where selective scribing of the upper Ti layer has been successfully fulfilled in continuous 0.1 × 0.1 and 0.5 × 0.5 cm^2 square patterns. OM and SEM images for 0.1 × 0.1 cm^2 ablation patterns are specified in Figure S7.

EDAX data obtained precisely from the ablated laser spot also confirmed the selective ablation of the Ti layer. SEM images show the post-CBD outcome of the given substrate, where selective NR growth in a grid-like manner has been obtained. The scanty rod-like growth observed in the nonablated regions is due to the 150 ns pulse duration of the laser system, which is a relatively long ablation period for metal thin films that have a heat transfer period of a few femtoseconds. The second sample set has been prepared via scribing the deposited thin films under 25 W, 5500 mm·s^{-1}, and 70 kHz system parameters, which correspond to the final fluence energy of 28.4 J·cm^{-2}. The applied fluence energy is enormously high for any selective ablation and, therefore, completely removes the multilayered thin film from the surface along with the continuous 0.5 × 0.5 cm^2 square pattern. Figure 6B gives the OM and SEM images obtained as a result of high fluence energy ablation. The EDAX analysis received exactly from the laser spots proves the complete absence of any traces of either Zn or Ti atoms. The presence of Si, Mg, Na, C, and O elements testifies that the ablation energy has extended deep into the glass. SEM images have exhibited a different

https://dx.doi.org/10.1021/acsanm.0c01034
ACS Appl. Nano Mater. 2020, 3, 5881−5897

nanostructure growth inside the same CBD solution. Here, NFs are grown in the center of the laser scribed spot region, while scanty NR growth in the perimeters of the spot can be observed due to the remaining molten ZnO.

The investigation of the interaction between the laser beam and thin film has been studied in detail via computational simulation by using COMSOL Multiphysics Heat Transfer module (License No.: 17077178). Computations have been conducted by using eqs S3−S5 (parameters are elaborated in Table S3) to quantify the temperature distribution throughout the successive thin-film layers. A detailed explanation of computational simulation analyses has been given elsewhere.[67] As mentioned above, the fluence energy variation has been maintained through changing the power, frequency, and scan rate of the laser beam. Parts C and D of Figure 6 represent the gradual temperature rise on substrates concerning thin-film thicknesses within a 95 ns pulse duration period for 3.7 and 28.4 J·cm^{-2} fluence energies, respectively. The spot radius of the incident laser beam has been designated as 20 μm, and the material absorption coefficient and reflectivity values have been calculated according to eqs S6 and S7 specified in the Supporting Information.

The insets given in Figures 6C,D are the cross-sectional representatives of temperature distribution throughout the thin-film deposited substrates under 1064 nm laser pulse. A highly significant difference can be observed between two fluence energies, where the highest temperature reached for 28.4 J·cm^{-2} exceeds that of 3.7 J·cm^{-2} by almost 7-fold. This result is a confirmative outcome explaining the reason for variation between two ablation parameters, where 3.7 J·cm^{-2} penetrates until ZnO but does not damage it and 28.4 J·cm^{-2} is strong enough to pierce until the glass substrate. Studies based on laser-ablated thin-film scribing reported in the literature so far support our modeling outcomes by reaching highly elevated temperatures under various fluence energy values.[68−70]

The variations in material properties of patterned samples have been investigated via PL and UV−vis spectroscopic analyses and specified in Figure 7. Analyzing the PL spectra obtained from pristine, 0.1 × 0.1 cm^2, and 0.5 × 0.5 cm^2 patterned NR samples (Figure 7A), a substantial difference can be observed from the luminescence intensities. Pristine NR film possesses a significantly low PL intensity, which sharply increases after patterning. This phenomenon can be attributed to the increased surface area of the samples contributing to higher responses. A distinguishable difference between two different pattern dimensions can also be observed. Simultaneous examination of PL data with the SEM images can be helpful for the proper interpretation of this difference. Although a significant laser-ablated alley for rod growth can be observed from SEM images of 0.1 × 0.1 cm^2 patterned samples, the distance between spot features is too small. Since the heat transfer during the ns laser period is high enough for nanoscale metal thin films, a possible thinning might occur between the laser scribed features. Therefore, at the CBD step, this thinned metal film does not play as a successful ZnO growth inhibitor as it is supposed to be. Hence, a partially homogeneous NR growth can be observed throughout the substrate.

The situation differs for 0.5 × 0.5 cm^2 substrates where the distance between laser-ablated features is more significant, and therefore, more selective growth and stronger PL intensity have been obtained (Figure 6A). Figure 7B shows the PL spectra obtained from the pristine and ablated samples with the fluence energy of 28.4 J·cm^{-2}. In the given data, nonpatterned and 0.1 × 0.1 cm^2 samples show a similar luminescence behavior. This situation can also be explained via concurrently examining SEM images with the obtained PL spectra. As can be seen from the OM and SEM images of 0.1 × 0.1 cm^2 samples, the distances between spots are too close.

The reason behind this is the applied excess fluence energy on a substrate that results in expanse spots which have diameters ≥40 μm. Thus, in close patterning distance, laser-ablated features come into contact, leaving an impression of a hatched substrate. However, in the case of the 0.1 × 0.1 cm^2 ablation, there is still a trace amount of ZnO seed layer remaining on the surface, which can lead to a scanty growth of NRs throughout the substrate. Therefore, the resulting PL response reveals double NBE peaks, which are the contribution of both NR and NF films. In the case of a 0.5 × 0.5 cm^2 ablation pattern, the luminescence behavior of thin films completely changes. The obtained spectrum is the result of the equal contributions of PL responses from both rod and flake. This outcome proves that both morphologies possessing different luminescent abilities have been combined on the same substrate and that the simultaneous growth of two distinct morphologies within the same CBD solution has a remarkable contribution to the PL responses.

Moreover, from the combined NBE emission, it can be seen that each nanostructure preserves its individuality by generating a double-headed peak representing NR and NF from low to high wavelengths, respectively. In other words, NRs and NFs generate their characteristic NBEs with slightly blue and red inclinations. UV−vis spectra have been taken as a fortiori analysis to prove that changes in PL responses are mostly related to the changing absorption behavior of thin films. In Figure 7C and D, the absorbance of pristine samples started with a stronger absorption in UV, followed by a gradual decrease while approaching the visible region. As a result of patterning, the distances between morphology grown pathways enlarge eventuating in higher light-exposed surface area and thus stronger absorption. For NRs, the absorption behavior within the UV region does not substantially change, while an increased absorbance is observed within the visible wavelength range. On the other hand, NF samples show a slight drop in the UV region, followed by a stronger absorbance between 400 and 700 nm.

Due to the proven excellent quantum yield and high stability, Cs−Pb−Br composite materials, as one of the most outstanding IHP material in LED applications, have been used to sensitize the patterned ZnO thin films. In this way, the broad luminescence range of composite rod/flake structures has been aimed to be further improved via incorporation of all-inorganic lead halide perovskites into the structure. NF/NR grid samples have been deposited with perovskite material via the spin-coating method under two different conditions, where the synthesis has been initiated by altering the spin number of $PbBr_2$:CsBr precursor solutions from (I) 1:1 to (II) 1:5 ratios. The conversion into Cs rich form has been attained via postannealing step at 280 °C in ambient air.

Prepared samples have been further characterized and examined via fluorescence microscopy (FM), SEM, PL, UV−vis, and XRD methods. The primary FM analysis has been conducted under UV, blue, and green excitations for both pristine and perovskite deposited patterned samples, respectively. FM images obtained from bare ZnO grid samples before perovskite deposition are specified in Figure S8 for

https://dx.doi.org/10.1021/acsanm.0c01034
ACS Appl. Nano Mater. 2020, 3, 5881−5897

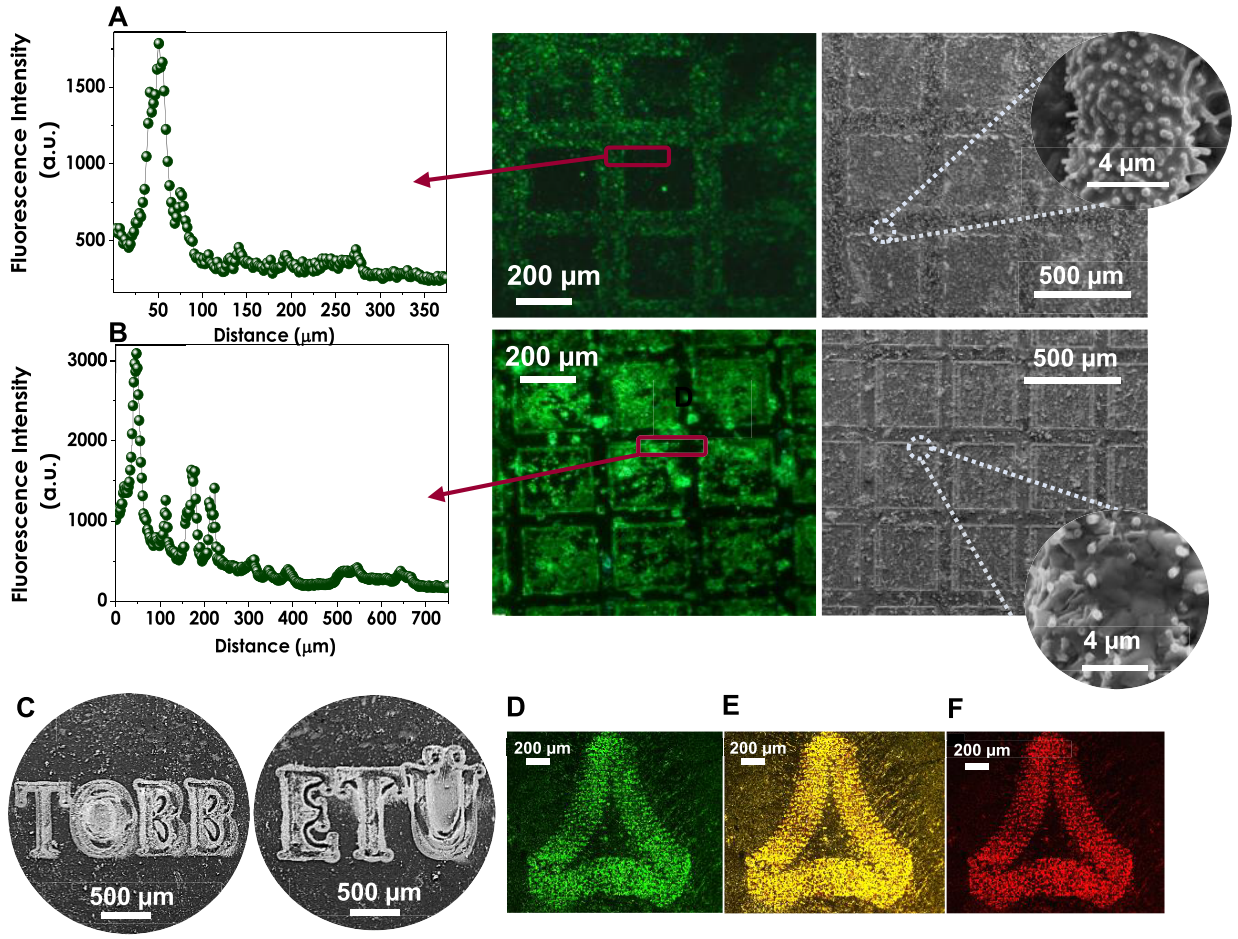

Figure 8. (A) Combined figure representing FM emission of 1:1 perovskite deposited ZnO grid samples with the corresponding intensity distribution along the marked region and SEM image obtained from the same sample with zooming toward the border region of the laser pattern showing the perovskite deposited rods. (B) Combined figure representing FM emission of 1:5 perovskite deposited ZnO grid samples with the corresponding intensity distribution along the marked region and SEM image obtained from the same sample with zooming toward the border region of the laser pattern where grain boundaries of crystal domains can be easily distinguished. (C) SEM image of the abbreviation of university name, with the ZnO nanorod deposited via CBD after laser patterning. (D) FM image of the perovskite deposited logo after laser patterning and ZnO nanorod deposition. OM image of the perovskite deposited logo after laser patterning and ZnO nanorod deposition with (E) yellow filter and (F) red filter.

comparison. In their bare forms, grid samples have a strong blue emission generated as a result of UV excitation (365 nm), which lies directly within their bandgap. On the other hand, perovskite deposited patterned samples have been investigated under blue excitation corresponding to λ = 470 nm, and green-emitting fluorescence images have been obtained (Figure 8A and B). The attained emission range is in agreement with the bandgap of Cs_4PbBr_6, showing no emission response under either UV or red excitation wavelengths.

It can be observed that the green emission of the 1:1 sample comes mostly from the laser-ablated pathway by analyzing the FM images of perovskite deposited samples individually. On the contrary, the luminescence of 1:5 perovskite deposited sample arises from the center of the square patterns. This fundamental difference is assumed to be originated from the variation in the crystalline sizes of different perovskite precursor ratios that are investigated below in detail. The additional plots attached to fluorescence images are the numerical expressions for the emission intensities obtained from certain regions of samples. Taking a closer look at the fluorescence plots, it can be observed that the intensity of green emission numerically decreases while approaching the darker regions.

For a more detailed investigation, the SEM images are incorporated into Figure 8A and B, showing the perovskite deposited patterned ZnO samples. Zoomed images represent the borders of patterned squares where the population of NRs increases due to the remaining molten ZnO. The bulky pile observed in the zoomed images represents the perovskite formation surrounding NR structures. It can be observed that more distinguishable grain boundaries are noticed for a 1:5 ratio by comparing both precursor ratios. Figure 8C shows the SEM image of the abbreviated name of the university (TOBB ETU) patterned on ITO/ZnO/Ti coated glass substrate where the selective scribing of the upper Ti layer resulted in the growth of NRs throughout the engraved writing. In a similar manner, the pattern of the university logo has also been scribed and consecutively deposited with NR and 1:5 ratio perovskite layers. The FM image obtained from the prepared logo sample given in Figure 8D shows the green luminescence obtained as a result of blue excitation. The contrast between perovskite accumulated and nonaccumulated regions can be easily noticed from the luminosities coming from and out of the

https://dx.doi.org/10.1021/acsanm.0c01034
ACS Appl. Nano Mater. 2020, 3, 5881−5897

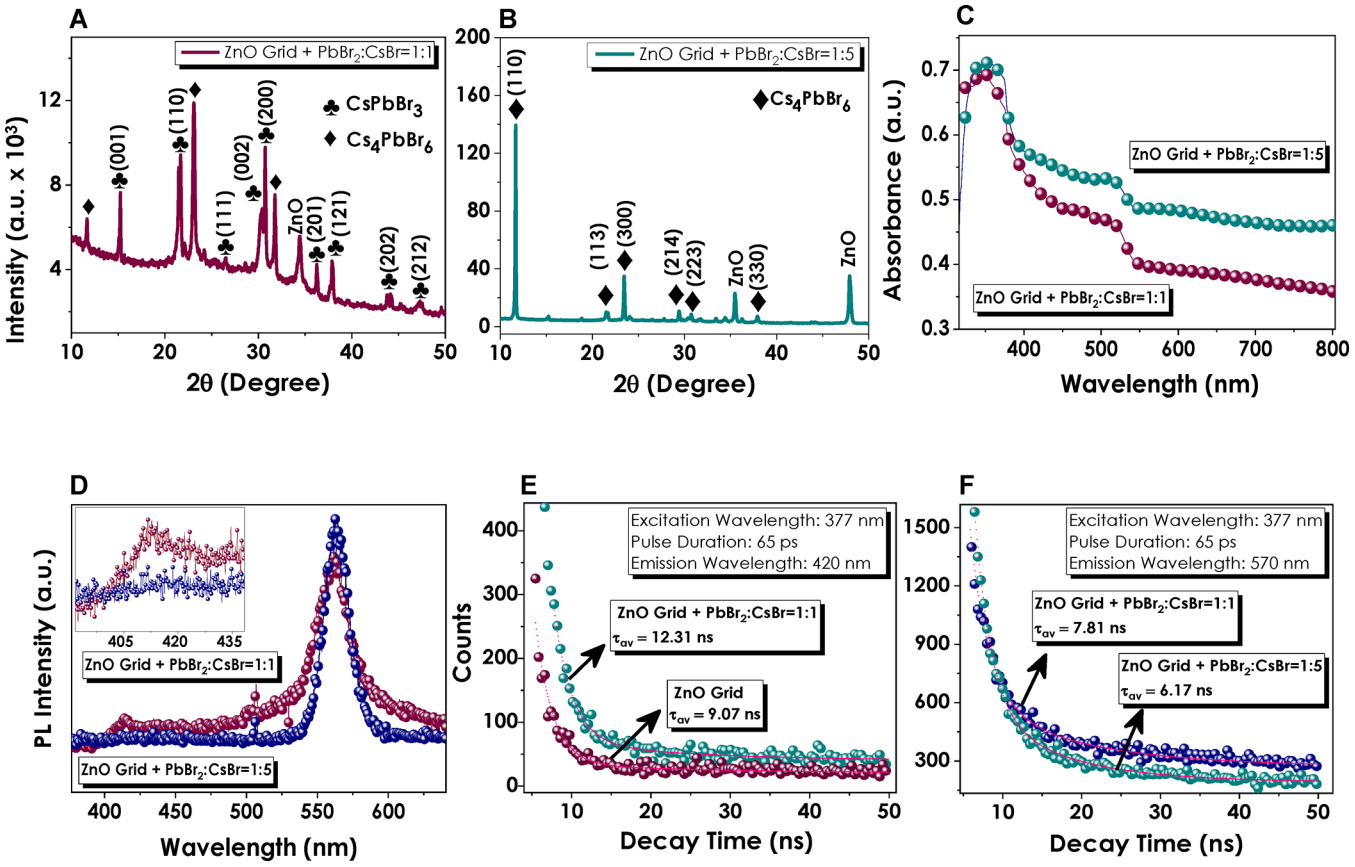

Figure 9. XRD spectra obtained from (A) 1:1 and (B) 1:5 spin number perovskite deposited ZnO with corresponding peak labels. (C) UV−vis spectrum of perovskite deposited ZnO grid samples with two significant excitonic absorption peaks each corresponding to the individual components of the thin film. (D) PL responses of perovskite deposited grid samples showing a suppressed defect-based ZnO emission due to the presence of severely luminescent perovskite. (E) TrPL plots of pristine and 1:1 perovskite deposited ZnO grid samples compared at 420 nm emission wavelength. (F) TrPL plots of 1:1 and 1:5 perovskite deposited grids with their individual comparison at characteristic 570 nm emission wavelength.

pattern, respectively. Besides, parts E and F of Figure 8 present the OM images obtained from the same sample under yellow and red filters, respectively. In principle, although both perovskites are synthesized from the same precursor solutions, the variation in ratios results in the formation of two different crystal structures.

A detailed investigation of the XRD spectra has been carried out on the given samples in order to determine their crystalline structures, which are directly correlated with the optical characteristics of the perovskite materials (Figure 9A and B). The XRD pattern of the (1:1) CsBr−$PbBr_2$ thin film shows that the perovskite layer bears two different phases which are (I) orthorhombic $CsPbBr_3$ and (II) rhombohedral Cs_4PbBr_6.[71] As previously reported, $CsPbBr_3$ has been observed to be converted into Cs_4PbBr_6 in the presence of excess Cs^+.[72,73] Thus, the spin-coating of as-prepared $PbBr_2$/CsBr precursors as 1:5 resulted in pure orthorhombic Cs_4PbBr_6 crystal phase formation. No characteristic diffraction peaks of $CsPbBr_3$ have been observed for the given thin films, which is possibly due to the small crystal size, low content, and good dispersion of $CsPbBr_3$ in the Cs_4PbBr_6 matrix.[74,75]

Moreover, a severe intensity variation can be observed for blend and pure Cs_4PbBr_6 crystal structures, which informs us about the crystal sizes of the obtained perovskites. Therefore, calculations have been performed for the determination of crystalline dimensions of Cs_4PbBr_6 structures showing that crystal sizes obtained from 1:5 samples are 4 times larger compared to those of 1:1. This can be proposed as a rationale behind the reason for 1:5 crystalline features being accumulated in the midsquares rather than laser-ablated pathways (Figure 8A and B). Optical properties and luminescence abilities of perovskite deposited grid thin films have been explored via UV−vis absorption and PL emission spectra, which are given in Figure 9C and D.

Obtained spectra reveal two significant excitonic absorption peaks located at 382 and 517 nm corresponding to the band edge positions of ZnO and Cs−Pb−Br perovskite layers, respectively. It has also been observed that the Cs_4PbBr_6 deposited ZnO thin film demonstrates superior absorption performance in the visible region compared to their pristine forms (Figure S9). The obtained enhancement at wavelengths >400 nm specifically points to the changing perovskite content, which has a stronger absorptivity throughout the visible region. The enhancement in absorption and luminescence properties of the ZnO nanostructured thin film supports the previously reported study based on $CsPbBr_3$ with ZnO NR systems.[76]

Analyzing the PL spectra of the patterned thin films having pure Cs_4PbBr_6 and $CsPbBr_3$−Cs_4PbBr_6 nanocomposite in Figure 9D, severe perovskite-originated emissions are found to almost hinder the luminescence of individual ZnO. Defect-based ZnO emissions are totally diminished for Cs_4PbBr_6 nanocomposite sensitized and patterned ZnO thin film

https://dx.doi.org/10.1021/acsanm.0c01034
ACS Appl. Nano Mater. 2020, 3, 5881−5897

obtained from 1:5 perovskite deposition. On the other hand, there is still a slightly noticeable peak from $CsPbBr_3$−Cs_4PbBr_6 sensitized patterned ZnO thin film at ∼420 nm signifying the characteristic ZnO-originated NBEs in 1:1 perovskite deposited sample. In addition, $CsPbBr_3$−Cs_4PbBr_6 nanocomposite sensitization via 1:1 perovskite deposition resulted in a broader peak, while the overall peak intensity of Cs_4PbBr_6 on patterned ZnO was noticeably higher.[77,78] The broadening in the dominant peak at 550 nm after 1:1 perovskite deposition might be the result of the wide-ranged PL luminescence of the ZnO nanostructure under perovskite material. This peak sharpens and gets stronger when the perovskite material transforms to Cs_4PbBr_6 nanocomposite, surprising the luminescence of the ZnO nanostructure.

It is important to note that each PL data set is compared with its counterparts obtained at the same slit number (0.01 nm). TrPL analysis has been conducted on the given samples in order to elucidate the changes in minority charge carrier lifetimes as a result of perovskite deposition. Pairwise comparison has been performed between pristine and 1:1 perovskite deposited ZnO grid samples for emissions obtained at 420 nm in Figure 9E. Both data have been fitted with a biexponential function with two decay times (τ_1 and τ_2) from which an average charge carrier lifetime has been calculated and specified in the figure inset.

Both pristine and 1:1 perovskite deposited ZnO grid films possess a fast primary decay component, which is 2.24 and 2.12 ns, respectively. As previously mentioned above, studies report the fast decay to be originated by radiative recombination in NBE of ZnO. On the other hand, second decay components, being 15.90 ns for pristine and 22.49 ns for 1:1 perovskite deposited ZnO samples, are assumed to represent the defect-related emissions generated at grain boundaries. The study reported by Li et al. has investigated the changes in charge carrier lifetimes of perovskites after ZnO incorporation.[79] It has been mentioned in the given study that the small grain sizes (i.e., large numbers of grain boundaries) result in an enhancement in defect-based recombination due to the increased trap densities. Considering that emission at 420 nm is the characteristic ZnO generated luminescence, the given lifetime increase can be directly attributed to the changing ZnO properties as a result of perovskite deposition.

The deposition of the perovskite layer on ZnO thin films required several heating steps as a result of which considerable differences are expected to occur in crystalline sizes. Therefore, by using Scherrer's equation, the crystal size evaluation on characteristic ZnO peak at 34.2° (2θ) diffraction angle has been conducted. The outcome of the following calculation, which is specified in Figure S10 and eq S8 of the Supporting Information in detail, shows a considerable diminution (by ∼3-fold) in the crystal size of ZnO as a result of perovskite deposited postannealing. Thus, the increase in trap assisted decay component can be considered to be originated by reduced ZnO crystal sizes. This can also be approved via comparing PL intensities of pristine and 1:1 perovskite deposited ZnO samples under the same slit number and at 420 nm where an enhancement of approximately 8-fold can be observed (Figure S11).

Also, the lifetime performances of 1:1 and 1:5 perovskite deposited ZnO thin films have been compared by contrasting their characteristic emissions at 570 nm (Figure 9F). Similar to the PL spectra, the obtained lifetime periods are pretty close to each other, generating almost similar fast primary decay components (τ_1(1:1 perovskite) = 2.4 ns; τ_1(1:5 perovskite) = 2.03 ns). However, a slower decay can be observed for both samples generated by nonradiative defect induced recombination where 1:1 perovskite samples predominate the decay lifetime of 1:5 by 3 ns (τ_2(1:1 perovskite) = 13.22 ns; τ_2(1:5 perovskite) = 10.21 ns). This small but significant difference is considered to be generated due to suppression of ZnO emission abilities under the denser perovskite layer of the 1:5 sample, which can also be confirmed through the PL spectra inset (Figure 9D).

CONCLUSIONS

In conclusion, the simultaneous growth of two different ZnO nanostructures has been attained in the same CBD solution by selectively altering substrate properties via NS fiber laser. The laser ablation has been performed in a controlled manner at predetermined fluence energies of 3.7 and 28.4 $J{\cdot}cm^{-2}$. The ablation parameters have been simulated via COMSOL Multiphysics to evaluate the approximate substrate temperatures under incident laser beam theoretically. Under low and high fluence energies, the substrate temperatures have been calculated to reach ∼2200 and ∼14000 K, respectively, explaining the penetration depth of each laser spot. The low fluence energy provided the selective scribing of the upper Ti layer, while, under high power throughputs, all of the consecutively deposited thin-film layers have been hatched from the surface. Combining these two scribing features on one substrate, the selective and patterned growth of ZnO NR and NF has been concurrently achieved. Consequently, the luminescence characteristics of both nanostructures have been combined in one substrate extending the emission range throughout the visible region and enhancing the composite PL intensities by approximately 7-fold. Besides, the charge carrier lifetimes have been increased by 7 ns, having an ultimate impact on PL performance. The final PL performance leap has been achieved with IHP sensitization of multimorphological ZnO thin films by reaching the highest carrier lifetime of 12.31 ns and enhancing the PL intensity by 4.7-fold. The remarkable performances obtained from the combination of easily synthesized, multimorphological ZnO, and composite-perovskite systems will shed light on the future applicability of these materials in optoelectronic systems and light-emitting devices.

ASSOCIATED CONTENT

Supporting Information

The Supporting Information is available free of charge at https://pubs.acs.org/doi/10.1021/acsanm.0c01034.

Details of NS fiber laser parameters and related equations, elaborated equations and variables of the COMSOL Multiphysics heat module, supplementary SEM, OM, and FM images, and supporting material characterization figures and tables (PDF)

AUTHOR INFORMATION

Corresponding Authors

Mehmet Sankir − *Micro and Nanotechnology Graduate Program and Department of Materials Science and Nanotechnology Engineering, TOBB University of Economics and Technology, 06560 Ankara, Turkey;* orcid.org/0000-0003-2103-0439; Email: mehmetsankir@gmail.com, msankir@etu.edu.tr

https://dx.doi.org/10.1021/acsanm.0c01034
ACS Appl. Nano Mater. 2020, 3, 5881−5897

Nurdan Demirci Sankir − *Micro and Nanotechnology Graduate Program and Department of Materials Science and Nanotechnology Engineering, TOBB University of Economics and Technology, 06560 Ankara, Turkey*; Email: ndsankir@gmail.com, nsankir@etu.edu.tr

Authors

Nazrin Abdullayeva − *Micro and Nanotechnology Graduate Program, TOBB University of Economics and Technology, 06560 Ankara, Turkey*

Cigdem Tuc Altaf − *Micro and Nanotechnology Graduate Program, TOBB University of Economics and Technology, 06560 Ankara, Turkey*

Alihan Kumtepe − *Micro and Nanotechnology Graduate Program, TOBB University of Economics and Technology, 06560 Ankara, Turkey*

Nazmi Yilmaz − *Department of Electrical and Electronics Engineering, TOBB University of Economics and Technology, 06560 Ankara, Turkey*

Ozlem Coskun − *Micro and Nanotechnology Graduate Program, TOBB University of Economics and Technology, 06560 Ankara, Turkey*

Hamza Kurt − *Micro and Nanotechnology Graduate Program, Department of Electrical and Electronics Engineering, and Department of Materials Science and Nanotechnology Engineering, TOBB University of Economics and Technology, 06560 Ankara, Turkey*

Cem Celebi − *Quantum Device Laboratory, Department of Physics, Izmir Institute of Technology, 35430 Izmir, Turkey*

Alper Yanilmaz − *Quantum Device Laboratory, Department of Physics, Izmir Institute of Technology, 35430 Izmir, Turkey*; orcid.org/0000-0001-5270-6695

Complete contact information is available at: https://pubs.acs.org/10.1021/acsanm.0c01034

Author Contributions

N.A., C.T.A., A.K., and O.C. performed the fabrication and characterization of samples. N.A. and C.T.A. contributed to the data analysis and preparation of the manuscript. N.Y. and H.K. carried out the FDTD simulations. A.Y. and C.C. performed the time-resolved photoconductivity experiments. N.D.S. and M.S. are the principal investigators of the study. N.D.S. and M.S. performed the data analysis. The manuscript was written through the contributions of all authors. All authors have given approval to the final version of the manuscript.

Notes

The authors declare no competing financial interest.

■ ACKNOWLEDGMENTS

This study was supported by The Scientific and Technological Research Council of Turkey (TUBITAK) under the research grants 315M348 and 119M030. The authors would like to thank The Turkish Atomic Energy Authority (TAEK) and Synchrotron-light for Experimental Science and Applications in the Middle East (SESAME) for X-ray absorption studies. Also, the authors would like to thank Isınsu Baylam from KOC University Surface Science and Technology Center for performing the time-resolved photoluminescence measurements.

■ REFERENCES

(1) Kang, H. W.; Yeo, J.; Hwang, J. O.; Hong, S.; Lee, P.; Han, S. Y.; Lee, J. H.; Rho, Y. S.; Kim, S. O.; Ko, S. H.; Sung, H. J. Simple ZnO Nanowires Patterned Growth by Microcontact Printing for High Performance Field Emission Device. *J. Phys. Chem. C* **2011**, *115* (23), 11435−11441.

(2) Lin, Y.; Lu, K.; Davis, R. Patterning of ZnO Quantum Dot and PMMA Hybrids with a Solvent-Assisted Technique. *Langmuir* **2019**, *35* (17), 5855−5863.

(3) Xu, S.; Wei, Y.; Kirkham, M.; Liu, J.; Mai, W.; Davidovic, D.; Snyder, R. L.; Zhong, L. W. Patterned Growth of Vertically Aligned ZnO Nanowire Arrays on Inorganic Substrates at Low Temperature without Catalyst. *J. Am. Chem. Soc.* **2008**, *130* (45), 14958−14959.

(4) He, H.; Hsu, J. H.; Wang, C. W.; Lih, H. N.; Chen, L. J.; Wang, Z. L. Pattern and Feature Designed Growth of ZnO Nanowire Arrays for Vertical Devices. *J. Phys. Chem. B* **2006**, *110* (1), 50−53.

(5) Kristensen, A.; Yang, J. K. W.; Bozhevolnyi, S. I.; Link, S.; Nordlander, P.; Halas, N. J.; Mortensen, N. A. Plasmonic Colour Generation. *Nat. Rev. Mater.* **2017**, *2*, 16088.

(6) Inan, H.; Poyraz, M.; Inci, F.; Lifson, M. A.; Baday, M.; Cunningham, B. T.; Demirci, U. Photonic Crystals: Emerging Biosensors and Their Promise for Point-of-Care Applications. *Chem. Soc. Rev.* **2017**, *46* (2), 366−388.

(7) Khanikaev, A. B.; Shvets, G. Two-Dimensional Topological Photonics. *Nat. Photonics* **2017**, *11*, 763−773.

(8) Li, G.; Zhang, S.; Zentgraf, T. Nonlinear Photonic Metasurfaces. *Nat. Publ. Gr.* **2017**, *2*, 1−14.

(9) Liu, J.; Zhao, H.; Wu, M.; Van der Schueren, B.; Li, Y.; Deparis, O.; Ye, J.; Ozin, G. A.; Hasan, T.; Su, B.-L. Slow Photons for Photocatalysis and Photovoltaics. *Adv. Mater.* **2017**, *29*, 1605349.

(10) Huang, X.; Guo, Q.; Kang, S.; Ouyang, T.; Chen, Q.; Liu, X.; Xia, Z.; Yang, Z.; Zhang, Q.; Qiu, J.; Dong, G. Three-Dimensional Laser-Assisted Patterning of Blue-Emissive Metal Halide Perovskite Nanocrystals inside a Glass with Switchable Photoluminescence. *ACS Nano* **2020**, *14*, 3150.

(11) Fang, M.; Dong, G.; Wei, R.; Ho, J. C. Hierarchical Nanostructures: Design for Sustainable Water Splitting. *Adv. Energy Mater.* **2017**, *7*, 1700559.

(12) Yang, Y.; Niu, S.; Han, D.; Liu, T.; Wang, G.; Li, Y. Progress in Developing Metal Oxide Nanomaterials for Photoelectrochemical Water Splitting. *Adv. Energy Mater.* **2017**, *7*, 1700555.

(13) Zheng, X.; Zhang, L. Photonic Nanostructures for Solar. *Energy Environ. Sci.* **2016**, *9*, 2511−2532.

(14) Ou, Q.; Li, Y.; Tang, J. Light Manipulation in Organic Photovoltaics. *Adv. Sci.* **2016**, *3*, 1600123.

(15) Haug, F.-J.; Ballif, C. Light Management in Thin Film Silicon Solar Cells. *Energy Environ. Sci.* **2015**, *8*, 824−837.

(16) Wang, H.-P.; Lien, D.-H.; Tsai, M.-L.; Lin, C.-A.; Chang, H.-C.; Lai, K.-Y.; He, J.-H. Photon Management in Nanostructured Solar Cells. *J. Mater. Chem. C* **2014**, *2*, 3144−3171.

(17) Geng, C.; Wei, T.; Wang, X.; Shen, D.; Hao, Z. Enhancement of Light Output Power from LEDs Based on Monolayer Colloidal Crystal. *Small* **2014**, *10* (9), 1668−1686.

(18) Zhmakin, A. I. Enhancement of Light Extraction from Light Emitting Diodes. *Phys. Rep.* **2011**, *498* (4−5), 189−241.

(19) Zhao, F.; Ma, D. Approaches to High Performance White Organic Light-Emitting Diodes for General Lighting. *Mater. Chem. Front.* **2017**, *1*, 1933−1950.

(20) Kang, G.; Yoo, J.; Ahn, J.; Kim, K. Transparent Dielectric Nanostructures for Efficient Light Management in Optoelectronic Applications. *Nano Today* **2015**, *10* (1), 22−47.

(21) Kathalingam, A.; Vikraman, D.; Karuppasamy, K.; Kim, H.; Park, H.; Shanmugam, K. Materials Science in Semiconductor Processing Maskless Patterned Growth of ZnO Nanorod Arrays Using Tip Based Electrolithography. *Mater. Sci. Semicond. Process.* **2018**, *77*, 24−30.

(22) Chen, K.; Chen, K.; Thang, D. D.; Ishii, S.; Sugavaneshwa, R. P. Selective Patterned Growth of ZnO Nanowires/Nanosheets and Their Photoluminescence Properties Selective Patterned Growth of ZnO Nanowires/Nanosheets and Their Photoluminescence Properties. *Opt. Mater. Express* **2015**, *5*, 353−360.

(23) Consonni, V.; Sarigiannidou, E.; Appert, E.; Bocheux, A.; Guillemin, S.; Donatini, F.; Robin, I. C.; Kioseoglou, J.; Robaut, F. Selective Area Growth of Well-Ordered ZnO Nanowire Arrays with Controllable Polarity. *ACS Nano* **2014**, *8* (5), 4761−4770.
(24) Hassanpour, A.; Bogdan, N.; Capobianco, J. A.; Bianucci, P. Hydrothermal Selective Growth of Low Aspect Ratio Isolated ZnO Nanorods. *Mater. Des.* **2017**, *119*, 464−469.
(25) Park, S.-H.; Kim, S.-H.; Han, S.-W. Growth of homoepitaxial ZnO film on ZnO nanorods and light emitting diode applications. *Nanotechnology* **2007**, *18*, 055608.
(26) Wang, J. X.; Sun, X. W.; Yang, Y.; Huang, H.; Lee, Y. C.; Tan, O. K. Hydrothermally Grown Oriented ZnO Nanorod Arrays for Gas Sensing. *Nanotechnology* **2006**, *17*, 4995−4998.
(27) Wang, Z. L.; Song, J. Piezoelectric Nanogenerators Based on Zinc Oxide Nanowire Arrays. *Science (Washington, DC, U. S.)* **2006**, *312*, 242−246.
(28) Jiao, M.; Viet, N.; Van Duy, N.; Duc, N. On-Chip Hydrothermal Growth of ZnO Nanorods at Low Temperature for Highly Selective NO_2 Gas Sensor. *Mater. Lett.* **2016**, *169*, 231−235.
(29) Li, L.; Gu, L.; Lou, Z.; Fan, Z.; Shen, G. ZnO Quantum Dot Decorated Zn_2SnO_4 Nanowire Heterojunction Photodetectors with Drastic Performance Enhancement and Flexible Ultraviolet Image Sensors. *ACS Nano* **2017**, *11* (4), 4067−4076.
(30) Lu, J.; Xu, C.; Li, F.; Yang, Z.; Peng, Y.; Li, X.; Que, M.; Pan, C.; Wang, Z. L. Piezoelectric Effect Tuning on ZnO Microwire Whispering-Gallery Mode Lasing. *ACS Nano* **2018**, *12* (12), 11899−11906.
(31) Jin, C.; Kim, H.; Ryu, H.; Kim, H. W.; Lee, C. Subwavelength Optical Resonant Cavity-Induced Enhancement of the Near-Band-Edge Emission from ZnO-Core/SnO_2-Shell Nanorods. *J. Phys. Chem. C* **2011**, *115*, 8513−8518.
(32) He, H.; Li, S.; Ye, Z. Improved Internal Quantum Efficiency of Photoluminescence in Zinc Ion-Implanted ZnO Bulk Crystals. *Appl. Phys. A: Mater. Sci. Process.* **2019**, *125* (4), 125−227.
(33) Hassan, A.; Jin, Y.; Azam, M.; Irfan, M.; Jiang, Y. Large Photoluminescence Enhancement in Mechanical-Exfoliated One-Dimensional ZnO Nanorods. *J. Mater. Sci.: Mater. Electron.* **2019**, *30*, 5170−5176.
(34) Yang, K.; Fu, J.; Hu, L.; Xiong, Z.; Li, M.; Wei, X.; Xiao, Z.; Lu, S.; Sun, K. Impact of ZnO Photoluminescence on Organic Photovoltaic Performance. *ACS Appl. Mater. Interfaces* **2018**, *10*, 39962−39969.
(35) Bora, T.; Sathe, P.; Laxman, K.; Dobretsov, S.; Dutta, J. Defect Engineered Visible Light Active ZnO Nanorods for Photocatalytic Treatment of Water. *Catal. Today* **2017**, *284*, 11−18.
(36) Chanda, A.; Gupta, S.; Vasundhara, M.; Joshi, S. R.; Mutta, G. R.; Singh, J. Study of Structural, Optical and Magnetic Properties. *RSC Adv.* **2017**, *7*, 50527−50536.
(37) Dai, S.; Wang, Y.; Zhang, D.; Han, X.; Shi, Q.; Shujie, W.; Du, Z. Fabrication of Surface-Patterned ZnO Thin Films Using Sol-Gel Methods and Nanoimprint Lithography Fabrication of Surface-Patterned ZnO Thin Films Using Sol−Gel Methods and Nanoimprint Lithography. *J. Sol-Gel Sci. Technol.* **2011**, *60*, 17−22.
(38) Yeo, J.; Hong, S.; Kim, G.; Lee, H.; Suh, Y. D.; Park, I.; Grigoropoulos, C. P.; Ko, S. H. Laser-Induced Hydrothermal Growth of Heterogeneous Metal-Oxide Nanowire on Flexible Substrate By. *ACS Nano* **2015**, *9* (6), 6059−6068.
(39) Lee, H.; Yeo, J.; Lee, J.; Cho, H.; Kwon, J.; Han, S.; Kim, S.; Hong, S.; Ko, S. H. Selective Thermochemical Growth of Hierarchical ZnO Nanowire Branches on Silver Nanowire Backbone Percolation Network Heaters. *J. Phys. Chem. C* **2017**, *121*, 22542−22549.
(40) Murillo, G.; Rodr, I.; Esteve, J. Selective Area Growth of High-Quality ZnO Nanosheets Assisted by Patternable AlN Seed Layer for Wafer-Level Integration. *Cryst. Growth Des.* **2016**, *16*, 5059−5066.
(41) Wang, Y.; Wei, X. Y.; Kuang, S. Y.; Li, H. Y.; Chen, Y. H.; Liang, F.; Su, L.; Wang, Z. L.; Zhu, G. Triboelectrification-Induced Self-Assembly of Macro-Sized Polymer Beads on a Nanostructured Surface for Self-Powered Patterning. *ACS Nano* **2018**, *12* (1), 441−447.
(42) Abdullayeva, N.; Altaf, C. T.; Mintas, M.; Ozer, A.; Sankir, M.; Kurt, H.; Sankir, N. D. Investigation of Strain Effects on Photoelectrochemical Performance of Flexible ZnO Electrodes. *Sci. Rep.* **2019**, *9* (1), 1−14.
(43) Liu, Z.; Ya, J.; Lei, E. Effects of Substrates and Seed Layers on Solution Growing ZnO Nanorods. *J. Solid State Electrochem.* **2010**, *14* (6), 957−963.
(44) Tanaka, I.; Mizoguchi, T. First-Principles Calculations of X-ray Absorption near Edge Structure and Energy Loss near Edge Structure: Present and Future. *J. Phys.: Condens. Matter* **2009**, *21*, 104201.
(45) Liu, H.; Zeng, F.; Gao, S.; Wang, G.; Song, C.; Pan, F. Contributions of Magnetic Properties in Epitaxial Copper-Doped ZnO. *Phys. Chem. Chem. Phys.* **2013**, *15* (31), 13153−13161.
(46) Xin, J.; Chang, C. M.; Hsueh, C. H.; Lee, J. F.; Chen, J. M.; Lin, H. H.; Lu, N.; Ferguson, I. T.; Guan, Y.; Wan, L.; Yang, Q.; Feng, Z. C. X-Ray Absorption Fine Structure of ZnO Thin Film on Si and Sapphire Grown by MOCVD. *2016 5th Int. Symp. Next-Generation Electron. ISNE 2016* **2016**, 5−6.
(47) Jeong, E. S.; Yu, H. J.; Han, S. W.; An, S. J.; Yoo, J.; Kim, Y. J.; Yi, G. C. Local Structural Properties of ZnO Nanoparticles, Nanorods and Powder Studied by Extended X-Ray Absorption Fine Structure. *J. Korean Phys. Soc.* **2008**, *53* (1), 461−465.
(48) Decremps, F.; Datchi, F.; Saitta, M.; Polian, A.; Pascarelli, S.; Di Cicco, A.; Itié, P.; Baudelet, F. Local Structure of Condensed Zinc Oxide. *Phys. Rev. B: Condens. Matter Mater. Phys.* **2003**, *68*, 104101.
(49) Yan, D.; Zhang, W.; Cen, J.; Stavitski, E.; Sadowski, J. T.; Vescovo, E.; Walter, A.; Attenkofer, K.; Stacchiola, D. J.; Liu, M. Near Band Edge Photoluminescence of ZnO Nanowires: Optimization via Surface Engineering. *Appl. Phys. Lett.* **2017**, *111*, 231901.
(50) Wang, T.; Zhang, X.; Wen, J.; Chen, T.; Ma, X.; Gao, H. Diameter-Dependent Luminescence Properties of ZnO Wires by Mapping. *J. Phys. D: Appl. Phys.* **2014**, *47* (17), 175304.
(51) Lv, Y.; Zhang, Z.; Yan, J.; Zhao, W.; Zhai, C.; Liu, J. Growth Mechanism and Photoluminescence Property of Hydrothermal Oriented ZnO Nanostructures Evolving from Nanorods to Nanoplates. *J. Alloys Compd.* **2017**, *718*, 161−169.
(52) Ghose, S.; Rakshit, T.; Ranganathan, R.; Jana, D. Role of Zn-Interstitial Defect States on D0 Ferromagnetism of Mechanically Milled ZnO Nanoparticles. *RSC Adv.* **2015**, *5* (121), 99766−99774.
(53) Eswar, K. A.; Husairi, F. S.; Ab Aziz, A.; Rusop, M.; Abdullah, S. Photoluminescence Spectra of ZnO Thin Film Composed Nanoparticles on Silicon and Porous Silicon. *Adv. Mater. Res.* **2013**, *832*, 843−847.
(54) Djurišić, A. B.; Leung, Y. H. Optical Properties of ZnO Nanostructures. *Small* **2006**, *2* (8−9), 944−961.
(55) Göpel, W.; Lampe, U. Influence of Defects on the Electronic Structure of Zinc Oxide Surfaces. *Phys. Rev. B: Condens. Matter Mater. Phys.* **1980**, *22* (12), 6447−6462.
(56) Neshchimenko, V.; Li, C.; Mikhailov, M.; Lv, J. Optical Radiation Stability of ZnO Hollow Particles. *Nanoscale* **2018**, *10* (47), 22335−22347.
(57) Raji, R.; Gopchandran, K. G. ZnO Nanostructures with Tunable Visible Luminescence: Effects of Kinetics of Chemical Reduction and Annealing. *J. Sci. Adv. Mater. Devices* **2017**, *2* (1), 51−58.
(58) Gheisi, A. R.; Neygandhi, C.; Sternig, A. K.; Carrasco, E.; Marbach, H.; Thomele, D.; Diwald, O. O_2 Adsorption Dependent Photoluminescence Emission from Metal Oxide Nanoparticles. *Phys. Chem. Chem. Phys.* **2014**, *16* (43), 23922−23929.
(59) Fan, H. B.; Yang, S. Y.; Zhang, P. F.; Wei, H. Y.; Liu, X. L.; Jiao, C. M.; Zhu, Q. S.; Chen, Y. H.; Wang, Z. G. Investigation of Oxygen Vacancy and Interstitial Oxygen Defects in ZnO Films by Photoluminescence and X-Ray Photoelectron Spectroscopy. *Chin. Phys. Lett.* **2007**, *24* (7), 2108−2111.
(60) Chang, F. M.; Brahma, S.; Huang, J. H.; Wu, Z. Z.; Lo, K. Y. Strong Correlation between Optical Properties and Mechanism in Deficiency of Normalized Self-Assembly ZnO Nanorods. *Sci. Rep.* **2019**, *9* (1), 1−9.

https://dx.doi.org/10.1021/acsanm.0c01034
ACS Appl. Nano Mater. 2020, 3, 5881−5897

(61) Khokhra, R.; Bharti, B.; Lee, H. N.; Kumar, R. Visible and UV Photo-Detection in ZnO Nanostructured Thin Films via Simple Tuning of Solution Method /639/301/1005 /639/301/357/551 /140/146 Article. *Sci. Rep.* **2017**, *7* (1), 1−14.
(62) Wang, M.; Zhou, Y.; Zhang, Y.; Jung Kim, E.; Hong Hahn, S.; Gie Seong, S. Near-Infrared Photoluminescence from ZnO. *Appl. Phys. Lett.* **2012**, *100*, 101906.
(63) Han, N. S.; Shim, H. S.; Seo, J. H.; Kim, S. Y.; Park, S. M.; Song, J. K. Defect States of ZnO Nanoparticles: Discrimination by Time-Resolved Photoluminescence Spectroscopy. *J. Appl. Phys.* **2010**, *107*, 084306.
(64) Yoshikawa, H.; Adachi, S. Optical Constants of ZnO. *Jpn. J. Appl. Phys.* **1997**, *36*, 6237−6243.
(65) Özdoğan, M.; Yiğen, S.; Çelebi, C.; Utlu, G. The Comparison of Transient Photocurrent Spectroscopy Measurements of Pulsed Electron Deposited ZnO Thin Film for Air and Vacuum Ambient Conditions. *Thin Solid Films* **2019**, *680* (April), 48−54.
(66) Sarkar, S.; Basak, D. Understanding of Ultraviolet Photoresponse Properties of ZnO Nanorods: Effect of Nanorod's Size and Ambient. *J. Nanosci. Lett.* **2015**, *5* (4), 1−4.
(67) McDonnell, C.; Milne, D.; Chan, H.; Rostohar, D.; O'Connor, G. M. Part 1: Wavelength Dependent Nanosecond Laser Patterning of Very Thin Indium Tin Oxide Films on Glass Substrates. *Opt. Lasers Eng.* **2016**, *80*, 73−82.
(68) Torrisi, L.; Gammino, S.; Andò, L.; Nassisi, V.; Doria, D.; Pedone, A. Comparison of Nanosecond Laser Ablation at 1064 and 308 nm Wavelength. *Appl. Surf. Sci.* **2003**, *210* (3−4), 262−273.
(69) Hamad, A. H.; Khashan, K. S.; Hadi, A. A. Laser Ablation in Different Environments and Generation of Nanoparticles. *Applications of Laser Ablation - Thin Film Deposition, Nanomaterial Synthesis and Surface Modification*; IntechOpen: London, 2016; pp 177−196. DOI: 10.5772/65241.
(70) Mcdonnell, C.; Milne, D.; Chan, H.; Rostohar, D.; O'Connor, G. M. Part 2: Ultra-Short Pulse Laser Patterning of Very Thin Indium Tin Oxide on Glass Substrates. *Opt. Lasers Eng.* **2016**, *81*, 70−78.
(71) Xu, L.; Li, J.; Fang, T.; Zhao, Y.; Yuan, S.; Dong, Y.; Song, J. Synthesis of Stable and Phase-Adjustable $CsPbBr_3$@Cs_4PbBr_6 Nanocrystals: Via Novel Anion-Cation Reactions. *Nanoscale Adv.* **2019**, *1* (3), 980−988.
(72) De Weerd, C.; Lin, J.; Gomez, L.; Fujiwara, Y.; Suenaga, K.; Gregorkiewicz, T. Hybridization of Single Nanocrystals of Cs_4PbBr_6 and $CsPbBr_3$. *J. Phys. Chem. C* **2017**, *121* (35), 19490−19496.
(73) Wu, L.; Hu, H.; Xu, Y.; Jiang, S.; Chen, M.; Zhong, Q.; Yang, D.; Liu, Q.; Zhao, Y.; Sun, B.; Zhang, Q.; Yin, Y. From Nonluminescent Cs_4PbX_6 (X = Cl, Br, I) Nanocrystals to Highly Luminescent $CsPbX_3$ Nanocrystals: Water-Triggered Transformation through a CsX-Stripping Mechanism. *Nano Lett.* **2017**, *17* (9), 5799−5804.
(74) Chen, Y. M.; Zhou, Y.; Zhao, Q.; Zhang, J. Y.; Ma, J. P.; Xuan, T. T.; Guo, S. Q.; Yong, Z. J.; Wang, J.; Kuroiwa, Y.; Moriyoshi, C.; Sun, H. T. Cs_4PbBr_6/$CsPbBr_3$ Perovskite Composites with Near-Unity Luminescence Quantum Yield: Large-Scale Synthesis, Luminescence and Formation Mechanism, and White Light-Emitting Diode Application. *ACS Appl. Mater. Interfaces* **2018**, *10* (18), 15905−15912.
(75) Chen, X.; Zhang, F.; Ge, Y.; Shi, L.; Huang, S.; Tang, J.; Lv, Z.; Zhang, L.; Zou, B.; Zhong, H. Centimeter-Sized Cs_4PbBr_6 Crystals with Embedded $CsPbBr_3$ Nanocrystals Showing Superior Photoluminescence: Nonstoichiometry Induced Transformation and Light-Emitting Applications. *Adv. Funct. Mater.* **2018**, *28* (16), 1706567.
(76) Zhang, H.; Wu, C.; Zhang, C.; Yan, B.; Guo, J.; Zhu, G.; Dai, J. P-GaN/n-ZnO Nanorod/$CsPbBr_3$ Quantum Dots Decorated with ZnO Nanoseeds for Light-Emitting Diodes. *ACS Appl. Nano Mater.* **2019**, *2* (12), 7661−7668.
(77) Qin, Z.; Dai, S.; Hadjiev, V. G.; Wang, C.; Xie, L.; Ni, Y.; Wu, C.; Yang, G.; Chen, S.; Deng, L.; Yu, Q.; Feng, G.; Wang, Z. M.; Bao, J. Revealing the Origin of Luminescence Center in 0D Cs_4PbBr_6 Perovskite. *Chem. Mater.* **2019**, *31*, 9098.
(78) Yang, L.; Li, D.; Wang, C.; Yao, W.; Wang, H.; Huang, K. Room-Temperature Synthesis of Pure Perovskite-Related Cs_4PbBr_6 Nanocrystals and Their Ligand-Mediated Evolution into Highly Luminescent $CsPbBr_3$ Nanosheets. *J. Nanoparticle Res.* **2017**, *19* (7). DOI: 10.1007/s11051-017-3959-7.
(79) Li, C.; Zang, Z.; Han, C.; Hu, Z.; Tang, X.; Du, J.; Leng, Y.; Sun, K. Enhanced Random Lasing Emission from Highly Compact $CsPbBr_3$ Perovskite Thin Films Decorated by ZnO Nanoparticles. *Nano Energy* **2017**, *40*, 195−202.

https://dx.doi.org/10.1021/acsanm.0c01034
ACS Appl. Nano Mater. 2020, 3, 5881−5897